8-2022

Upscaling and Development of Linear Array Focused Laser Differential Interferometry for Simultaneous 1D Velocimetry and Spectral Profiling in High-Speed Flows

Kirk Davenport
University of Tennessee, Knoxville, kdavenp2@utk.edu

To the Graduate Council:

I am submitting herewith a thesis written by Kirk Davenport entitled "Upscaling and Development of Linear Array Focused Laser Differential Interferometry for Simultaneous 1D Velocimetry and Spectral Profiling in High-Speed Flows." I have examined the final electronic copy of this thesis for form and content and recommend that it be accepted in partial fulfillment of the requirements for the degree of Master of Science, with a major in Mechanical Engineering.

Zhili Zhang, Major Professor

We have read this thesis and recommend its acceptance:

Trevor Moeller, Hans DeSmidt

Accepted for the Council:
Dixie L. Thompson

Vice Provost and Dean of the Graduate School

(Original signatures are on file with official student records.)

Upscaling and Development of Linear Array Focused Laser Differential Interferometry for Simultaneous 1D Velocimetry and Spectral Profiling in High-Speed Flows

A Thesis Presented for the

Master of Science

Degree

The University of Tennessee, Knoxville

Kirk Michael Davenport

August 2022

Acknowledgments

First and foremost, I am extremely grateful to my wife Elizabeth and my two children Lucas and Oliver. Over the past couple of years they have shown me an incredible amount of support and understanding while my attention was often divided between a full time job and full time classes. Without their support this simply would not have been possible.

I would like to thank Dr. Mark Gragston for his guidance and support both in helping me to navigate the academic landscape and in terms of the technical expertise and knowledge he was always willing to take the time to share. I would also like to acknowledge and thank my graduate advisor Dr. Zhili Zhang as well as the members serving on my graduate committee Dr. Trevor Moeller and Dr. Hans DeSmidt.

Finally, I would like to thank the University of Tennessee and Dr. John Schmisseur for supporting my use of the educational assistance program in pursuit of this degree.

Abstract

In this research a new configuration of linear array-focused laser differential interferometry (LA-FLDI) is described. This measurement expands on previous implementations of LA-FLDI through the use of an additional Wollaston prism. This additional prism expands the typical single LA-FLDI column into two columns of FLDI point pairs. The additional column of probed locations allows for increased spatial sampling of frequency spectra as well as the addition of simultaneous wall normal velocimetry measurements. The new configuration is used to measure the velocity profile and frequency content across a Mach 2 turbulent boundary layer at six wall normal locations simultaneously. Features of the measured spectra are shown to agree with expectations and the obtained boundary layer velocity profile is compared with previously obtained PIV measurements. The increase in simultaneously probed points provided by LA-FLDI is ideal for impulse facilities where spatial scanning via measurement system translation is not possible for a single run and techniques such as PIV may not be feasible. Initial testing was also carried out to determine if FLDI-based velocimetry can provide reasonable velocity profiles for adverse pressure gradients and over distributed roughness. Finally, a prototype photodiode array is proposed to simplify the optical setup for LA-FLDI and initial test results are provided comparing the impulse response of the prototype array to that of the amplified photodetectors currently in use.

Table of Contents

List of Figures

Chapter 1

Introduction

Ground testing and evaluation are a critical part of the development of supersonic and hypersonic vehicles due to the expense and risks associated with flight tests. The low risk and repeatability afforded by ground test facilities do however present their own set of difficulties. Even at low Mach numbers, it has proven to be exceedingly difficult to construct and operate facilities capable of accurately reproducing true flight conditions. Particularly in the field of hypersonics, this difficulty approaches impossibility as required stagnation pressures and temperatures reach astonishing values. Likewise, by nature of the requirement to accelerate the air rather than the test article for most ground facilities, efforts to recreate tbe freestream noise and turbulence levels seen in flight have also presented a significant challenge [1]. As a result, it is typical for individual facilities to focus on matching only one or two flight parameters at a time (e.g. Mach number, flow enthalpy, freestream noise, flight duration, etc.). To obtain meaningful results which are able to inform useful predictions and relationships, it is critical that comparisons can be made between facilities of differing characteristics. It is therefore necessary to obtain accurate measurements of the flow characteristics in the facility freestream as well as those surrounding a given test article. Additionally, over the past decades, computational modeling has become a significant

contributor to bridging the gap between flight conditions and ground test capabilities. As such, ground test facilities have seen a growing utility in model validation testing for new and existing computational fluid models. As the fidelity and accuracy of these models increases, so does their need for higher accuracy and higher spatial and temporal fidelity obtained from validation tests. Thus, researchers and engineers are continuously pursuing new diagnostic techniques to enhance the measurement capabilities of ground-based facilities. This work will focus on two such parameters, namely turbulent spectral content and flow velocity. This will be done in an attempt to improve upon the existing instrumentation available for these measurements.

The accurate characterization of turbulent structures in supersonic and hypersonic flow is a key factor in quantifying the results from most ground testing efforts. It has been shown that freestream facility noise and turbulence will influence boundary layer growth and instabilities along a model [2]. It then becomes crucial to characterize the turbulence of these initial conditions if any attempts are to be made to use experimental results for the validation of computational models or for correlation with other works. The growth of turbulent structures and instabilities are also clearly important in understanding boundary layer transition from laminar to turbulent and for informing the characteristics of boundary layer interactions. Traditionally, quantitative measurements of turbulence have been made with instruments such as hot-wire anemometers and fast response pressure transducers [1, 3, 4]. Both of these instruments however face many common limitations. Among them, integration of the sensing elements into the appropriate location in the flow can be complex and costly

and can become prohibitive as the number of probed locations increases. While typically less pronounced for pressure transducer implementations, flow intrusion by the instruments themselves is also a factor of concern with both hot-wire probes and pressure transducers. Similarly, as a result of direct exposure to the fluid flow, sensor survivability becomes a significant concern in high speed flows. Particularly as the hypersonic regime is approached, high flow velocities and stagnation temperatures become significant challenges, especially for the delicate wires used in hot-wire anemometers. Perhaps of most significance here are the limitations on bandwidth. Hot-wire anemometers are typically limited to responses in the range of 25-50 kHz with similar ranges for many standard high speed pressure transducers [3]. While pressure transducers can be found with rated frequency responses up to 1 MHz, realistic measurement response becomes highly dependent on the installation and associated geometries [5].

Velocity is another important quantity that must be characterized in order to appropriately model fluid flow. This is especially true in the boundary layer where the velocity profile can provide a meaningful picture of how the flow is evolving. Particle Image Velocimetry (PIV) has long been a mainstay diagnostic for the characterization of supersonic flow fields. This technique can be highly successful when used in relatively low-speed flows and can even provide useful turbulence data in some scenarios. In high-speed flows, however, particle response time becomes a more significant limitation and uniform seeding becomes increasingly difficult. This is particularly true when attempting to characterize the growth of a thin boundary layer along a tunnel model. Seeding for PIV measurements has also proven

to be a sizable challenge for impulse facilities such as Ludweig tubes, further limiting the use of the diagnostic. Molecular tagging velocimetry (MTV) techniques are quite effective for boundary layer measurements but require expensive and complicated laser systems and seeding the flow with a gas.

Recent works [6, 7] have utilized focused laser differential interferometry (FLDI) and correlation analysis as a means to measure velocity without seeding any material into the flow. FLDI was first discussed by Smeets [8] and allows for high frequency ($\geq$ 1 MHz) non-intrusive flow disturbance measurements, most commonly providing scalar turbulent spectra associated with density fluctuations. Most importantly, FLDI measurements have minimal path integration across the flow field allowing for precise placement of measurement locations. These properties have made FLDI a valuable tool for measuring delicate flow features such as turbulence intensity and boundary layer transition.

Chapter 2

FLDI Overview

Focused laser differential interferometry (FLDI) is as the name suggests, an interferometric technique used to measure the differential path length of two laser beams. As mentioned in the previous chapter, the technique was originally developed by Smeets and George in the early 70's [8, 9]. Smeets describes several configurations of his interferometer setup, however, the simplest explanation of the technique can be understood by looking at the non-focused version (LDI). A diagram of the LDI setup from Smeets work can be found in Fig. 2.1. In this setup, a linearly polarized laser beam is passed through a Wollaston prism which splits the beam into two separate beams polarized orthogonal relative to each other. The Wollaston prism is placed at the focal point of the first lens in the assembly so that the two beams become parallel as they pass through the optic. The beams then pass through the test region before reaching a mirrored but identical lens and Wollaston prism pair. The two beams recombine after passing through the second prism and can then be passed through a linear polarizer oriented at 45° relative to the polarization axis of both beams. After passing through the polarizer, an interference pattern will be created based on the phase offset between the two beams. The setup can be adjusted for an infinite fringe condition in the interference pattern. The result will be a single beam of laser light with an

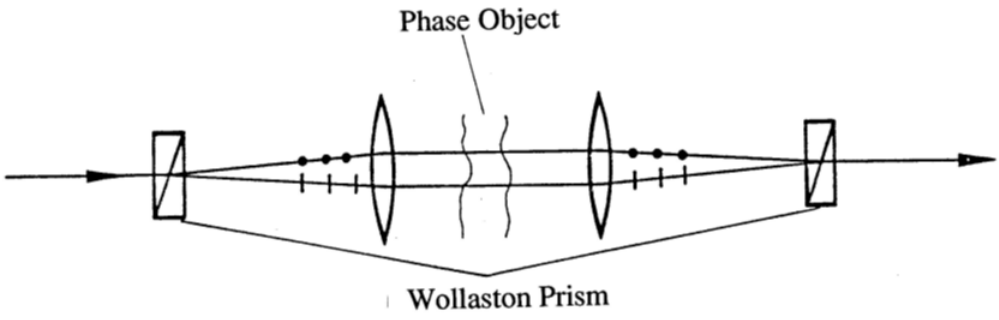

Figure 2.1: Simple dual beam laser differential interferometer comprised of a pair of Wollaston prisms and two lenses as drawn by Smeets [10].

intensity directly related to the difference in optical path between the two split beams. For an ideal setup, the length of the beam paths will be identical. The phase change between the two beams, $\Delta\phi$, is then limited to the difference in the integrated refractive index, n, and subsequent change in propagation speed between the two beam paths (s_1, s_2). This relationship is described by Eq. (2.1) below.

$$\Delta\phi = \frac{2\pi}{\lambda}\left(\int_{s_1} n_1\, ds - \int_{s_2} n_2\, ds\right) \tag{2.1}$$

By applying the Gladstone-Dale relationship ($n = K\rho + 1$) to Eq. (2.1), it can be shown that the configuration pictured in Fig. 2.1 is capable of measuring the integrated difference in gas density between the two beam paths (Eq. (2.2)).

$$\Delta\phi = \frac{2\pi K}{\lambda}\left(\int_{s_1} \rho_1\, ds - \int_{s_2} \phi_2\, ds\right) \tag{2.2}$$

For typical setups, the spacing between beam pairs, Δx, is kept as small as possible relative to the disturbance length scales. As a result, the output of the interferometer can be approximated as a finite-difference first derivative of the average density along a beam path of length L (Eqs. (2.3)).

$$\frac{\Delta\phi}{\Delta x}\frac{\lambda}{2\pi K L} = \frac{\int_{s_1} \rho_1\, ds - \int_{s_2} \rho_2\, ds}{\Delta x} \approx \frac{\partial\bar{\rho}}{\partial x} \tag{2.3}$$

Assuming both beams have the same initial intensity, $\frac{I_0}{2}$, the measured intensity after interference can be described by Eq. (2.4).

$$\frac{I}{I_0} = 1 + cos(\Delta\phi) \tag{2.4}$$

Traditionally the system will be adjusted to apply a DC phase offset of $-\pi/2$ between the two beams to avoid ambiguity caused by phase wrapping. For small phase disturbances, this offset also allows for the simplification of Eq. (2.4) by use of the small angle approximation as shown in Eq. (2.5).

$$\frac{I}{I_0} \approx 1 + \Delta\phi \tag{2.5}$$

Combining equations (2.3) and (2.5) provides a relationship between the measured intensity at the output of the instrument and the first derivative of average density change in the direction of the beam separation ((2.6)).

$$\left(\frac{I}{I_0} - 1\right) \frac{\lambda}{2\pi K L} \approx \frac{\partial \bar{\rho}}{\partial x} \tag{2.6}$$

Schmidt *et al.* [11] describe a system transfer function, $H(k)$, for LDI/FLDI systems in terms of density disturbance wavenumber, k. They define this function as the ratio of the instrument output to the true first derivative of the phase field. To allow for an analytical solution, $H(k)$ is computed for sinusoidal density fluctuations of infinitesimal

thickness propagating in the direction of beam separation. The transfer function is also broken down into the two components contributing to signal attenuation in the measurement. The first of these describes the response of the system, $H_w(k)$, resulting from the Gaussian beam diameter, w. The second, $H_s(k)$, describes filtering of the measured signal caused by the finite separation of the beam pairs, Δx. $H(k)$ can then be found through convolution of its individual components. Because the functions are defined in the wavenumber domain, this convolution can be carried out through simple multiplication. The resulting functions can be seen in Eqs. (2.7) - (2.9). A detailed derivation of these transfer functions can be found in [11] and [3].

$$H_w(k) = \exp(-\frac{w^2k^2}{8}) \tag{2.7}$$

$$H_s(k) = \frac{2\sin(\frac{k\Delta x}{2})}{k\Delta x} \tag{2.8}$$

$$H_w(k) = \frac{2}{k\Delta x}\sin(\frac{k\Delta x}{2})\exp(-\frac{w^2k^2}{8}) \tag{2.9}$$

The equations described above can also be applied to the focused version of this diagnostic (FLDI). For this variation, each of the two beam pairs is expanded prior to entering the test area such that both beams will have significantly increased diameters overlapping almost entirely at the focusing lens (collimating lens from the LDI system). This lens still serves the

original purpose of collimating the centerline path for both beams but provides an additional function for FLDI of focusing the expanded beams back to a point at the center of the test area. Because density variations will tend to be randomly distributed across a finite area, any signal from disturbance sizes on the order of the beam diameter or smaller will be heavily attenuated as describe by Eq. (2.7). Therefore, by expanding the beams prior to entering the test cell, it is possible to reject signal contributions from density fluctuations located away from the beam focus. For reference, Fig. 2.2 shows the Gaussian beam profile for a single beam passing through an FLDI setup with all of the beam splitting optics removed. Additional derivations and descriptions of the theory behind the FLDI measurement can be found in Refs. [3] and [11].

FLDI has largely been used as a method for detecting high-frequency spectral content in aerodynamic flow fields. It has been applied by Parziale to measure disturbances in a transitioning hyper-velocity boundary layer on a 5° half-angle cone, and to measure disturbance frequency content consistent with Mack modes and second-mode instability theory [12]. Bathel *et al.* [13] were also able to detect second-mode instability at Mach 6. The technique has also been applied to quantify tunnel free stream disturbance levels in the T5 shock tunnel at Caltech [14] and AEDC Tunnel 9 [3]. Recently, improvements to the FLDI technique have allowed measurements of the convective velocity of turbulent structures in supersonic flows using a correlation approach and two probe points created by the addition of a second beam splitting prism into the traditional optical setup [3, 6].

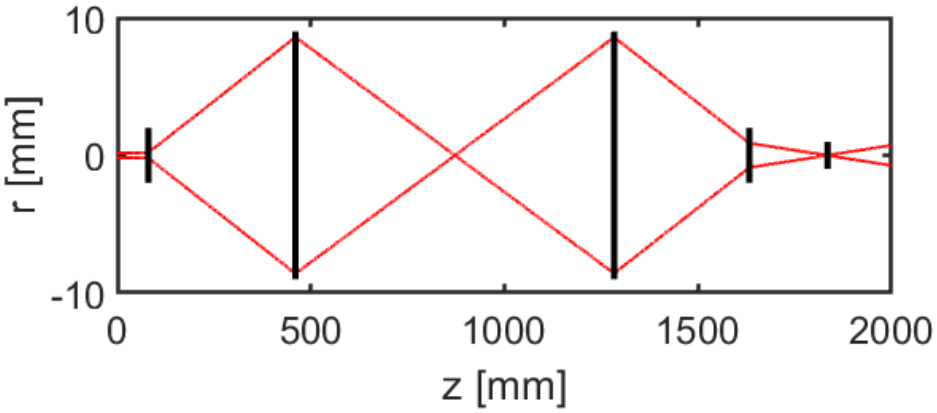

Figure 2.2: Gaussian beam path of an FLDI setup without the addition of any diffractive optics or Wollaston prisms. The beam expands through the primary optic and is then focused through a second lens down to a point in the test region before re-expanding and passing through the third lens to refocus the beam. A final lens is used to adjust the system focus onto the photodetectors.

Despite the advantages of FLDI, the technique has been significantly limited by its ability to probe only a single point. Whereas two-point FLDI doubles the number of spectral probing locations, this technique still only allows for a single velocity measurement. In facilities with long duration tests, it may be possible to translate the entire FLDI setup in order to probe multiple locations, but this would require significantly increased system complexity and does not allow for simultaneous correlation between the various probed locations. Furthermore, this technique would not be practical for impulse facilities such as Ludwieg tubes, shock tunnels, and expansion tunnels, which are facilities commonly used in modern hypersonic flow research. These limitations have made apparent the need for a more efficient and low-cost, multi-point FLDI technique in order to obtain simultaneous velocity and disturbance information across a larger spatial domain. In recent works by Gragston *et al.* [7, 15–17], this need was addressed with the introduction of Linear Array FLDI (LA-FLDI). In this method, a diffractive optical element was added to a typical FLDI setup, thereby splitting the beam into an array of six independent beams. These beams are then collected on the output of the FLDI setup by an array of fiber optic cables and sent to multiple photodetectors. The result at the focus of the FLDI setup is an array of six FLDI probe points that can provide disturbance measurements at multiple locations. Orientation of this array can also be easily manipulated by simple rotation of the diffractive element. The referenced work by Gragston *et al.* implements a six-point LA-FLDI system however any combination of array size and separation angle can be achieved with an appropriately designed diffractive optic.

It is worth noting that other variations of FLDI that enable multi-point measurements are being explored [18], highlighting the interest in increasing the number of probe locations.

In this work, LA-FLDI will be used to create two columns of six FLDI beam pairs that can simultaneously measure disturbance convective velocity and fluctuation spectra at multiple locations across a Mach 2 turbulent boundary layer. The resulting spectra will be analyzed to confirm that the data behaves as expected with the given flow conditions. The velocity profile measurements will also be compared with particle image velocimetry (PIV) data taken previously in the Mach 2 facility [19]. This work represents an extension of the concepts of both LA-FLDI and traditional dual-FLDI and could prove valuable for studying boundary layers in impulse facilities.

Chapter 3

Experimental Methodology

3.1 Facility Description and Conditions

Demonstration of the LA-FLDI velocimetry measurements was done using the UTSI Mach 2 blowdown tunnel depicted in Fig. 3.1. This facility was chosen because of the characterization work that has been carried out previously. Specifically, this work will take advantage of the existing PIV characterization of the boundary layer velocity profile as well as Schlieren imaging of the test section and boundary layer [19]. These will be used for validation of the LA-FLDI velocity measurements and boundary layer height estimation. Previously obtained schlieren images such as that pictured in Fig. 3.2 will also be used to ensure that the LA-FLDI measurement is taken sufficiently far away from any Mach or shock wave locations in the test section. The test section for this tunnel is 20.3 cm x 20.3 cm with three sequential sections each 40.64 cm in length. All measurements in this work will be carried out in the most upstream section. Air for the tunnel is fed by a 26.3 m^3 bottle farm. The maximum operating pressure of the bottle farm is 21 MPa and through procedural limits no more than 50% of the field capacity is used within a short period of

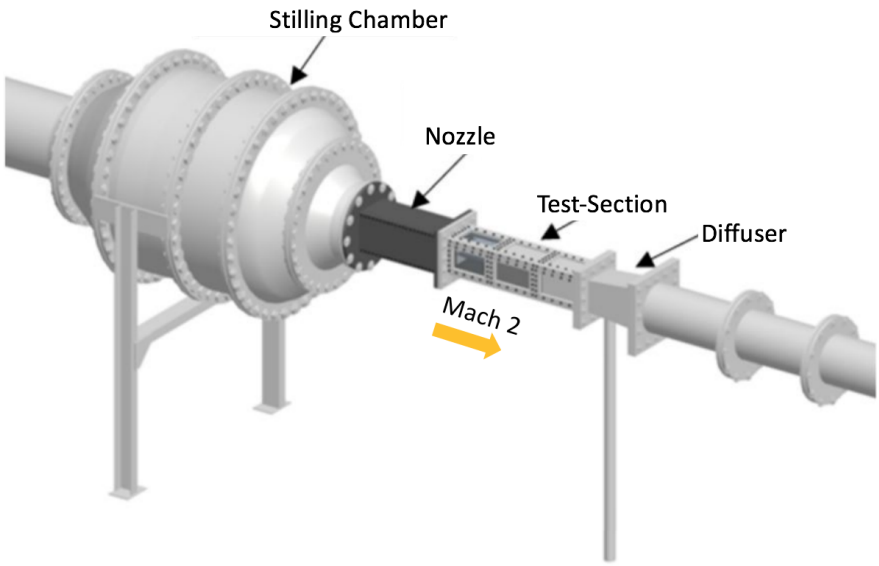

Figure 3.1: The UTSI Mach 2 wind tunnel.

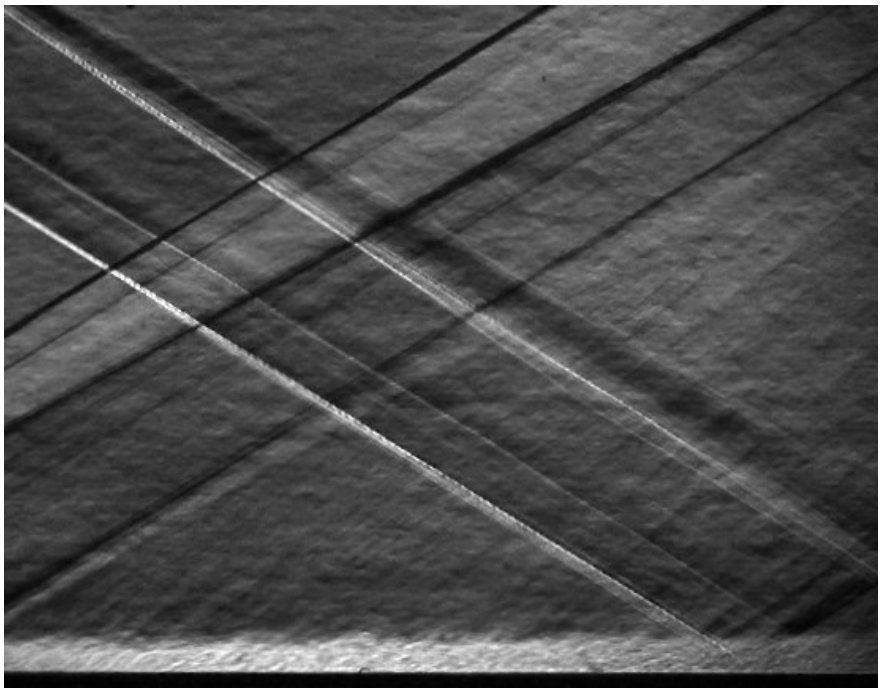

Figure 3.2: Schlieren Image of the UTSI M2 Freestream.

time (typically within a 4-8 hour period). Supply air is unheated and is assumed to start at roughly the ambient atmospheric temperature. Through the course of testing, it is expected that the supply air will cool as the pressure drops in the storage tanks and via expansion as test air crosses the pressure control valve. Given these parameters, the tunnel is capable of running multiple tests of approximately 15-20 seconds before refilling of the bottle farm is necessary. Testing for the primary experiment in this work was carried out in one day over the course of 4 separate tunnel runs. The initial bottle field pressure for these runs was 19.2 MPa and the final pressure after testing was recorded as 16.3 MPa. Ambient temperature during testing was approximately 297 K. The final temperature assuming no temperature recovery between runs is expected to be 293 K. This assumption is based on Eq. (3.1) where T_f and T_i are the initial and final air storage temperatures respectively and P_f and P_i are the respective initial and final storage pressures. The polytropic constant n is assumed to be 1.1 based on the bottle field geometry and configuration [20]. Nominal tunnel run parameters can be found in Table 3.1.

$$T_f = (\frac{P_f}{P_i})(\frac{n-1}{n}) \tag{3.1}$$

Optical access to the test section is available through a 31.8 cm x 14.0 cm ceiling window insert and two 31.8 cm x 17.8 cm wall inserts. For this experiment, a pair of BK7 windows were installed at the wall insert locations and a smooth steel insert was used at the ceiling location. The upstream test section also contains an interchangeable 33.0 cm x 7.6 cm floor

Table 3.1: Summary of nominal Mach 2 Tunnel Conditions.

P_0 [kPa]	T_0 [K]	U_∞ [m/s]	M_∞	Re_∞/x [m^{-1}]
210	285	507	2.01	30×10^6

plate for model mounting. For the primary experiment described here, a smooth floor insert flush with the tunnel floor was used.

3.2 LA-FLDI Setup

The optical setup for the LA-FLDI configuration used in this work is shown in Fig. 3.3. This setup uses a 10 mW HeNe laser beam (Lumentum 1135) with a beam diameter of 0.68mm and divergence of 1.2 mRad. The beam is expanded through an f = -9 mm plano-concave lens. The expanded beam is then passed through a linear polarizer (Thorlabs LPVISe100-A) and then through a diffractive optic (HOLO/OR MS-474-P-Y-A) designed to split the beam into six with a 0.71° separation angle. The six beams, distributed vertically, are then sent through a 30 mm x 30 mm 1.5° double Wollaston prism (United Crystal) where the beams are split into pairs of orthogonally polarized beams. This additional column of six beams created by this prism represents the second LA-FLDI array created by this setup. Next, the twelve beams are passed through a second polarizer (Thorlabs LPVISE200-A) oriented at 45 degrees relative to both incoming beam polarizations. At this point, all 12 beams will have the same polarization and the total laser power will have been reduced by approximately 50%. The 12 beams then pass through a 50 mm x 50 mm 1.5 arcminute Wollaston prism (United Crystals). This final prism splits each of the twelve beams into their respective orthogonally polarized FLDI pairs. The expanding beam pairs then pass through a final 75 mm diameter f = 200 mm plano convex focusing lens which will focus the expanded beams onto the measurement location and roughly collimate the optical axes

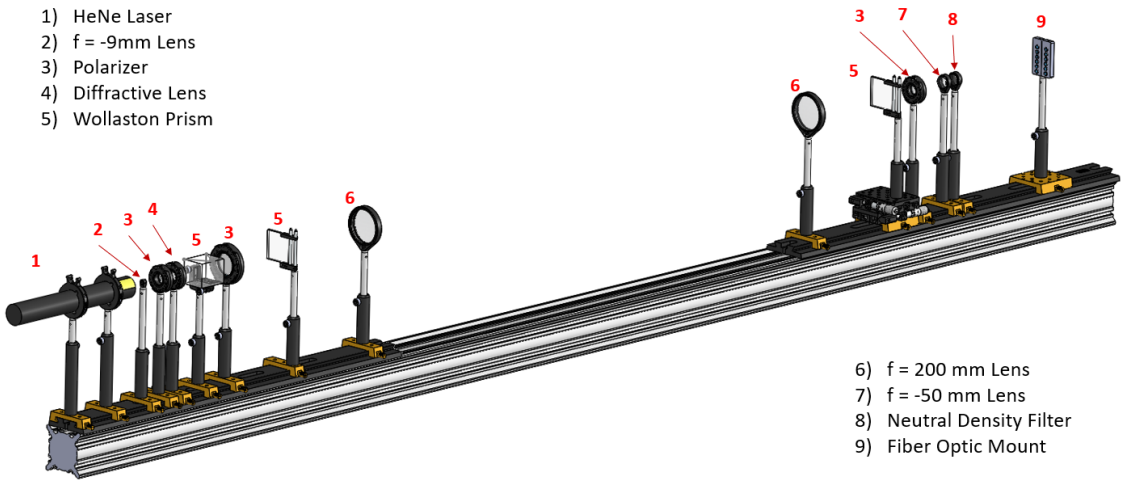

Figure 3.3: A CAD rendering of the LA-FLDI setup used in this work.

of each of now 24 beams as they pass through the test region. The collection side optics entail a 75 mm diameter f = 200 mm plano convex lens which will focus the 12 beam pairs onto a second 50 mm x 50 mm 1.5 arcminute Wollaston prism (United Crystals) where each pair will recombine spatially. The now 12 separate beams then pass through a third polarizer (Thorlabs LPVISE100-A) creating the 12 interference patterns that will become the signals for the experiment. A final f = -50 mm plano concave lens is used to focus the beams onto the signal collection optics. For this setup, each beam is captured by means of a fiber optic array. The array is comprised of 12 multimode fibers (Thorlabs M35L01) with collimators placed at the collection side. These carry the signals to 12 individual photodetectors (Thorlabs PDA36A2). Photodetector signals are collected by a National Instruments PXI system (NI PXIe-8381, NI BNC-2110, NI PXIe-6368) running at a 2 MHz acquisition rate. The theoretical optical paths calculated for this system are shown in Fig. 3.4 and 3.5.

Accurate measurement of the beam spacing at the system focus is crucial for obtaining meaningful data from the LA-FLDI setup. A beam profiler (Newport LBP2-VIS2) placed at the focal point of the FLDI system was used to collect the measurements of the beam pairs and beam pair locations relative to each other. As shown in Fig. 3.6, peak intensity locations were collected programmatically for each beam location and the necessary dimensions were then extracted based on the relative pixel locations and known sensor pixel size. Spacing between the two beams in an FLDI pair (96 μm) is used in the uncertainty analysis. The horizontal distance between each column of FLDI pairs (3.034mm) is used in the correlation

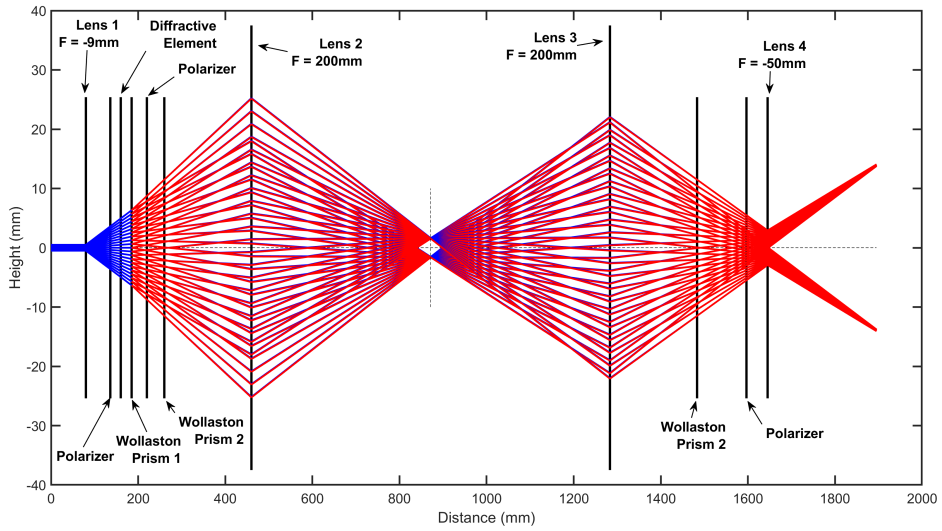

Figure 3.4: Output from geometric optics calculator for a top view of dual LA-FLDI. Note that the laser beam propagates from left to right.

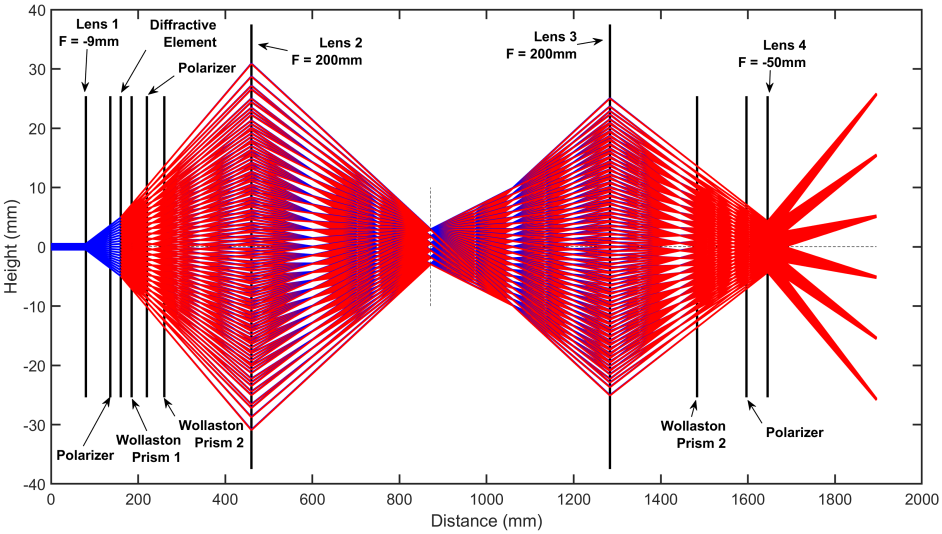

Figure 3.5: Output from geometric optics calculator for a side view of dual LA-FLDI. Note that the laser beam propagates from left to right.

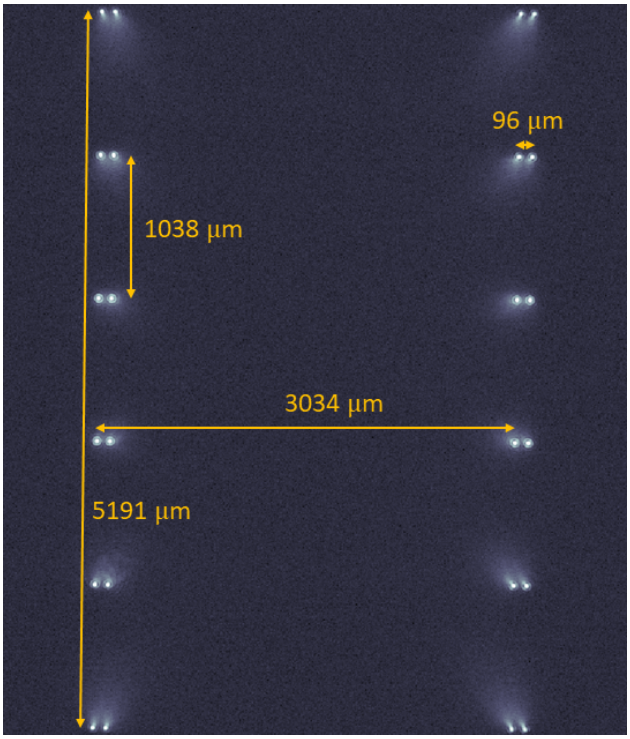

Figure 3.6: Beam profile at the focus of the LA-FLDI setup used for experiments.

analysis along with the corresponding signal lag to determine the flow velocity. The vertical spacing of 1.038mm between beam pairs is used for the determination of the measurement locations along with the overall column height of 5.191mm. The LA-FLDI assembly was setup on a single monolithic optical rail underneath the tunnel test section and mounted on vertical translation stages which allowed for accurate and repeatable vertical translation of the entire assembly. The setup is pictured in Fig. 3.7. For the initial test case, the array was positioned such that the lowest beam pairs were position 0.5mm above the test section floor as shown in Fig. 3.8. For each subsequent test case, the entire assembly was raised using the vertical translation stages and a precision machinists level was used to ensure that the rail remained level relative to the test section floor. For each vertical translation of the array in the tunnel, a reference measurement is taken to the lowest beam pair. The wall normal position for all measurement locations is then determined from the measured setup height along with the vertical beam pair spacing measured at the focus. In order to fully characterize the tunnel boundary layer, tests were carried out at four separate setup positions. At each setup position, three independent data sets were collected. The focal point of the array was centered in the test section with the optical axis normal to the flow direction. The distance between the nozzle exit and the centerline of the downstream LA-FLDI column was measured to be approximately 18.5cm. As mentioned previously, this location was selected to avoid proximity to any Mach waves or shock waves interacting with the tunnel floor. Fig. 3.9 shows a representation of the measurement locations relative to a previously collected schlieren image.

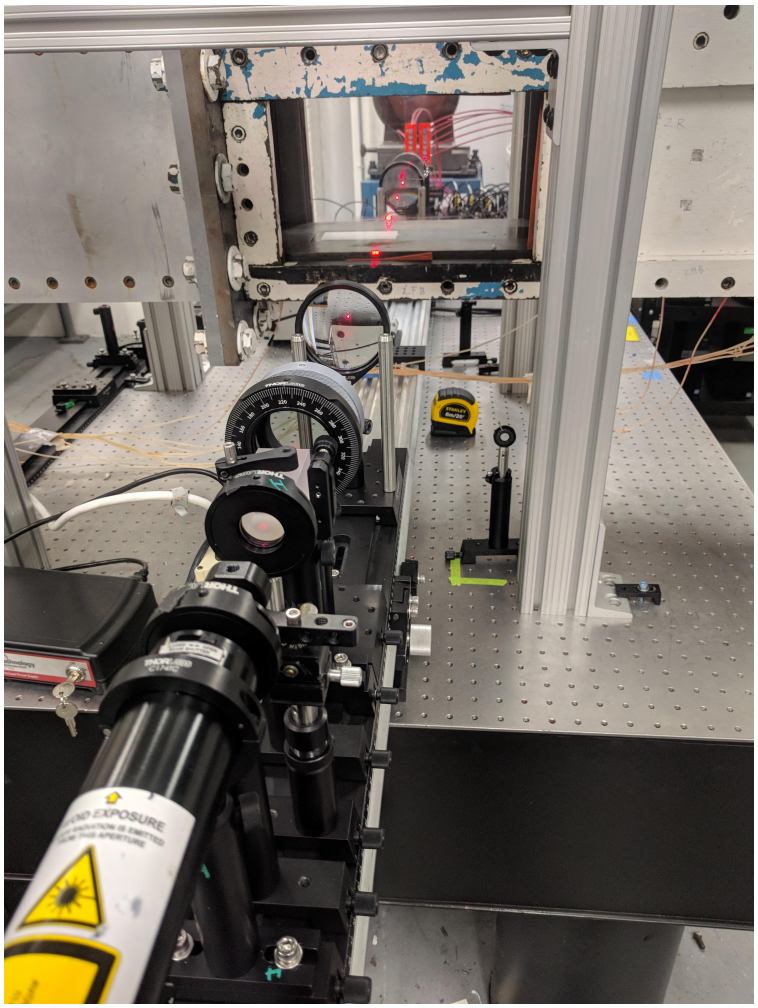

Figure 3.7: A photograph of the LA-FLDI setup under the Mach 2 test section.

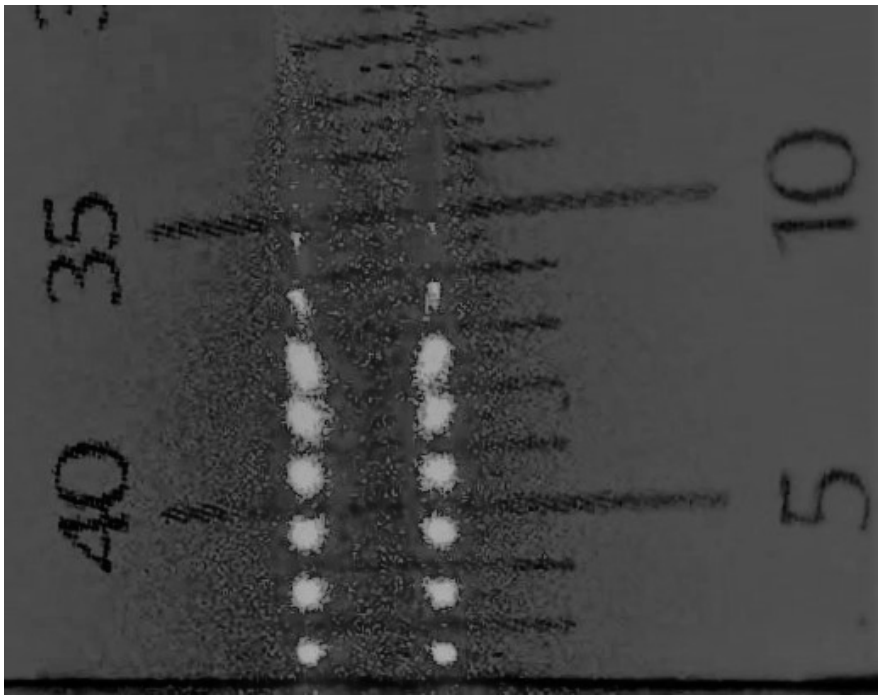

Figure 3.8: Image showing measurement of initial LA-FLDI measurement locations relative to the tunnel floor.

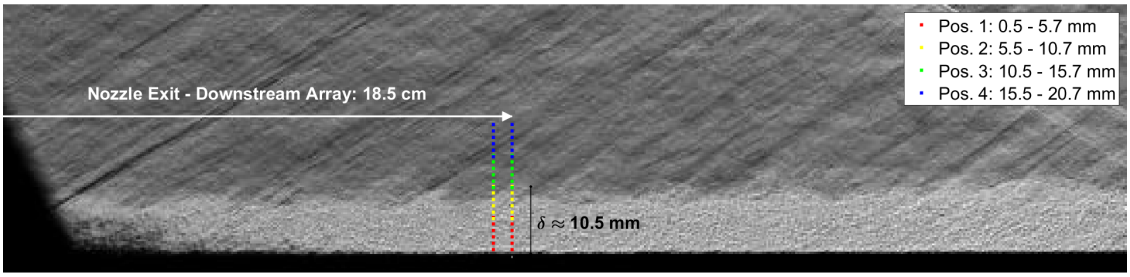

Figure 3.9: A schlieren image of the Mach 2 turbulent floor boundary layer with LA-FLDI probe locations annotated.

Prior to the collection of any data, the initial phase offset between the FLDI beam pairs was calibrated to be as close to $\pi/2$ as possible. To carry out this calibration, the signals from all 12 LA-FLDI channels were recorded while translating the final Wollaston prism perpendicular to the beams. In varying the position of the beams incident on the prism, a constant offset is applied to the phase difference between beam pairs. This measurement, shown in Fig. 3.10, was then used to find the maximum and minimum signal strength for each beam pair corresponding respectively to fully constructive and destructive interference (or phase offsets of 0 and π respectively). If seen in the collected data, these maximum and minimum intensity values would indicate the possibility of phase wrapping having occurred between the interfering beam pairs. The result of this would be an unacceptable ambiguity in the collected data. The prism is therefore placed at the position that brings each channel closest to their corresponding intensity midpoint. This position places the signals in the most linear portion of their range and minimizes the chance of a phase wrapping condition. Depending on the sensitivity of the LA-FLDI setup, however, it is still possible for a phase object with a high enough gradient to cross over the measurement location and cause a phase wrapping event. In order to test against this, each channel is checked following every test to verify that the measured signal envelope remained at least one standard deviation away from the corresponding peak intensity. A subset of voltage data and threshold values used in these verification tests is shown in Fig. 3.11.

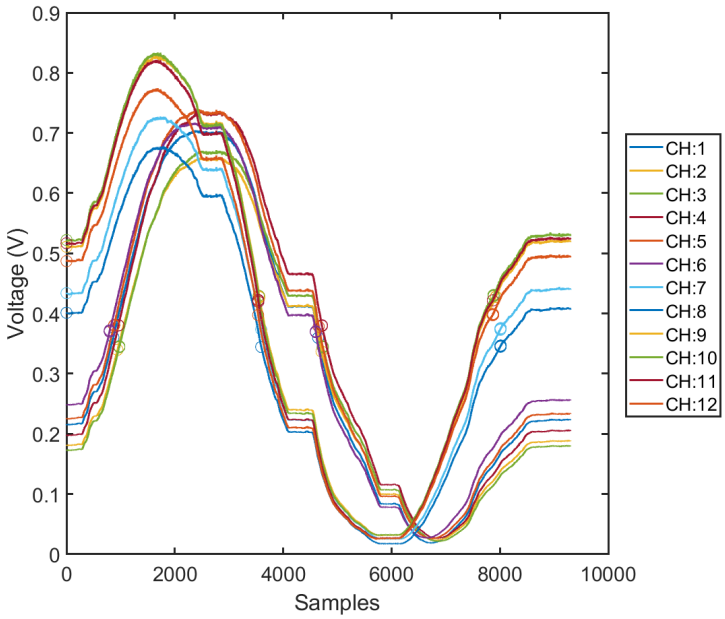

Figure 3.10: Plots showing the sinusoidal waveform obtained from translating the final Wollaston prism perpendicular to the primary optical axis. The maximum and minimum values indicate where phase wrapping and nonlinear response occur.

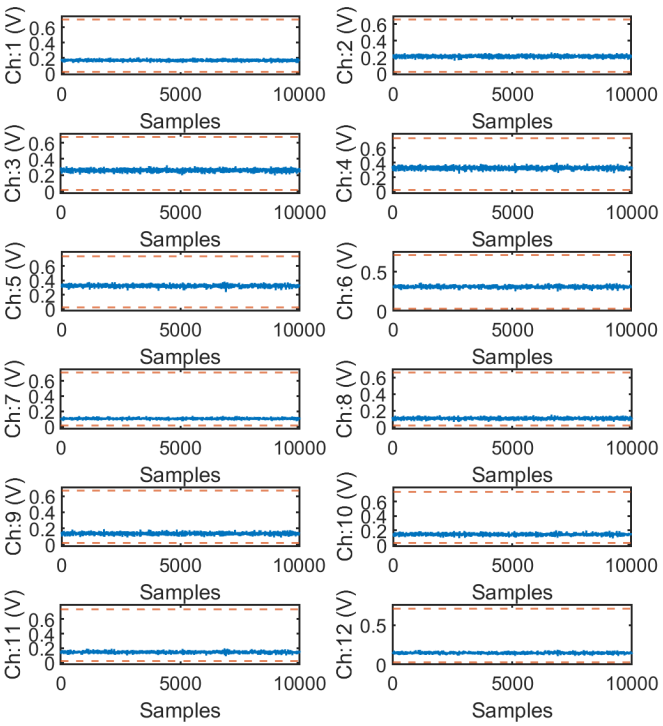

Figure 3.11: A subset of data collected on all 12 channels from tunnel Position 2 with corresponding phase limits.

Chapter 4

Results

4.1 Spectral Analysis

To demonstrate the ability of each FLDI beam in the 6×2 array to measure turbulent spectra, power spectral density (PSD) plots were created and analyzed for each of the 48 measurement locations. This analysis was done for each of the three independent data sets collected at each setup location. Additionally, background level data sets were collected and analyzed at each setup location. One of the ensuing challenges in analyzing this data was finding useful ways to represent the resulting 196 separate PSD's in a manner that would allow useful inferences to be made from the measurements. Independent data sets at each measurement location were typically compared to a single setup position at a time with separate plots for the upstream and downstream arrays (limiting each plot to no more than 24 data sets each) as seen in Fig. 4.1 and Fig. 4.2. As these plots were used for comparisons between data sets of the same channel in a single location, the data was analyzed prior to any normalization. Visualizations used in the analysis of the measured fluid dynamics were typically plotted for a single run across all 24 wall normal positions with separated plots for the upstream and

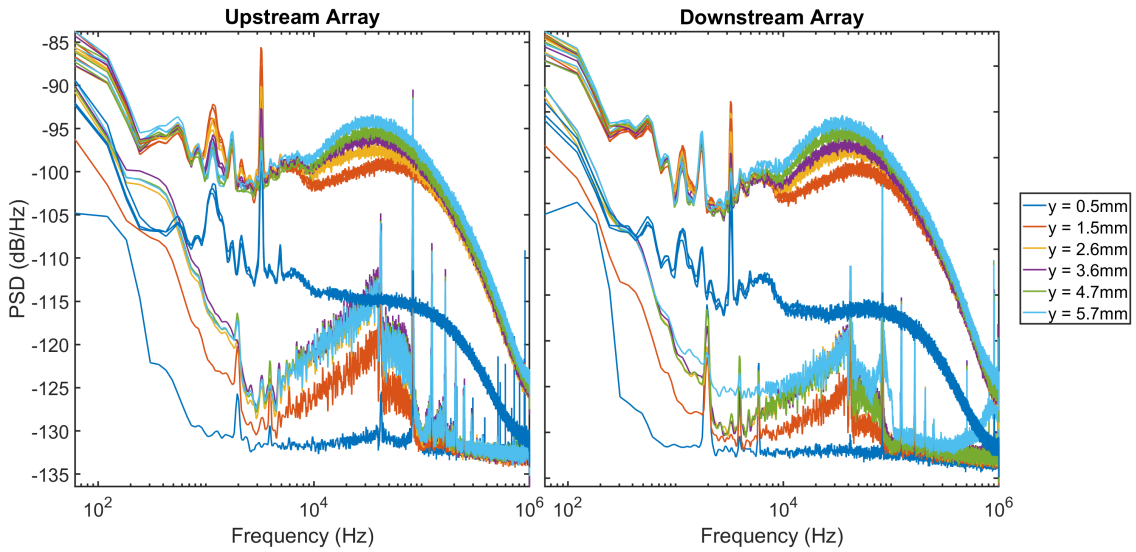

Figure 4.1: Power spectra for a subset of measurement Locations corresponding to the first setup location. Each plot shows spectra for all four data sets collected at this location. Each location retains the same plot color between data sets.

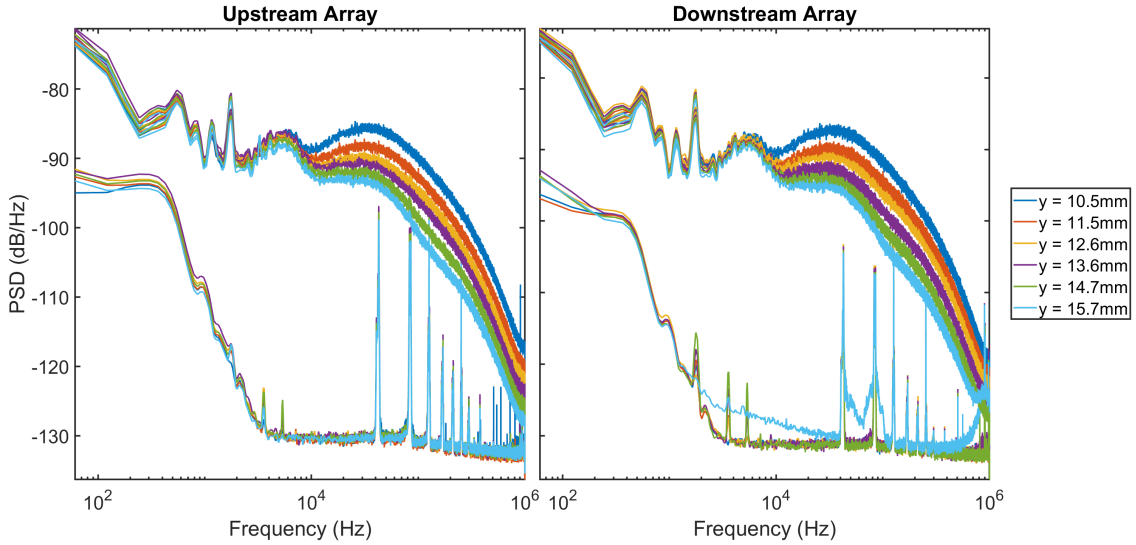

Figure 4.2: Power spectra for a subset of measurement Locations corresponding to the third setup location. Each plot shows spectra for all four data sets collected at this location. Each location retains the same plot color between data sets.

downstream array locations. Visualization of this type required normalization for accurate comparison between channels and setups. Several examples of these can be seen in Fig. 4.3 - 4.5 below. As a result of the large quantity of data collected in this work, it should be noted that the figures and data presented represent only a portion of the full data set collected. Those visualizations selected, however, provide an accurate summary of the significant trends seen within the data and were found to be consistent between individual data sets and tunnel runs. Another challenge, particularly in the analysis of the spectral content came with the selection of a normalization method for the PSD data. As mentioned previously, this became necessary to allow for meaningful comparison between the spectral content obtained from each measurement location without introducing excessive misrepresentation of the relative data. Variations in total power between the PSD measurements of different channels can be attributed to differences in the optical efficiency of the fiber optic collection array along with variations in the photodiodes themselves. Another cause for variation from a single channel between setup locations is the attenuation caused by a variable cutoff of the beam path by the tunnel floor. This effect results in higher median intensity values for measurements taken at setup locations farther from the tunnel floor. In order to normalize the resulting PSD data, an assumption was made that very low frequency (less than 100Hz) input would largely be dominated by 60 HZ AC electrical noise along with mechanical vibrations of the facility. This is supported by the significant low-frequency content in the background noise data and the expected increase in mechanical vibration during tunnel runs. Based on this

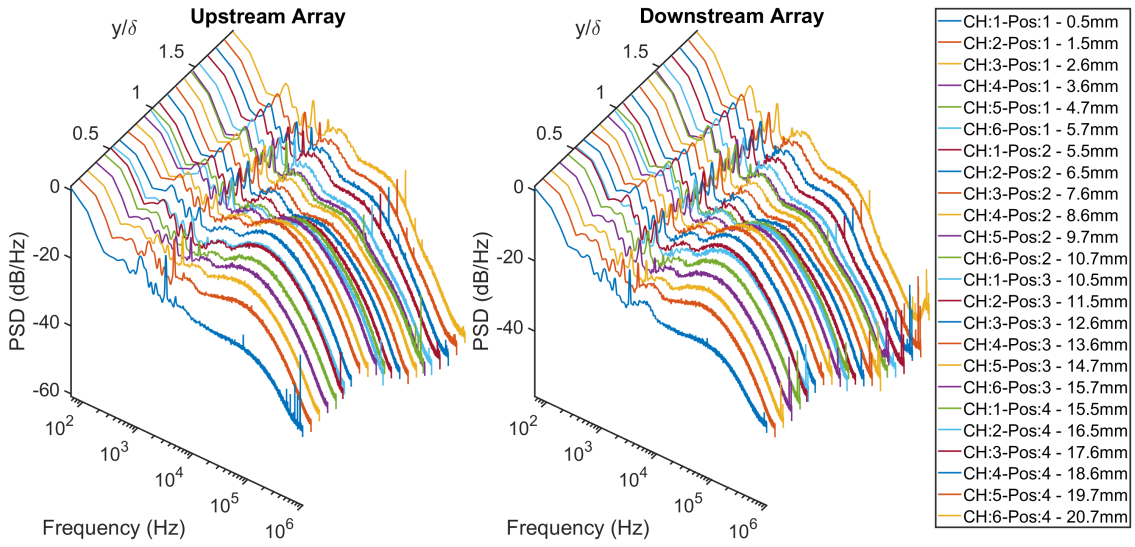

Figure 4.3: 3D Line plot of the normalized power spectra across all measurement locations. The boundary layer data shows the characteristic turbulent spectrum, which fades away in the freestream.

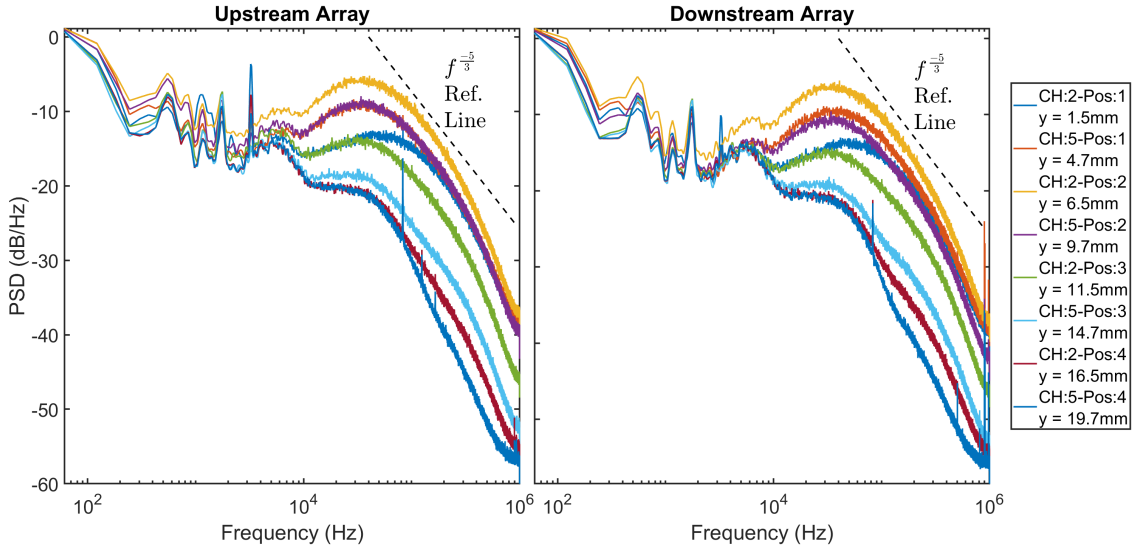

Figure 4.4: Normalized power spectra for a subset of measurement locations. The spectra in the freestream show much less content at higher frequencies and the characteristic peak of the boundary layer data matches the $\approx$ 46 kHz suggested by basic turbulence theory. Furthermore, similar trends are seen for upstream and downstream beam pairs.

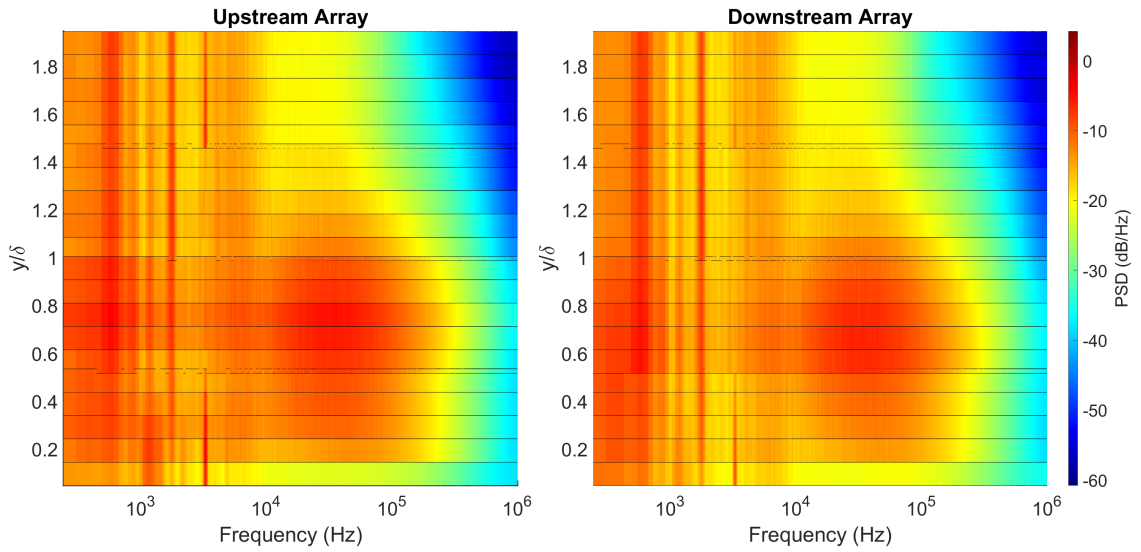

Figure 4.5: A colormap showing normalized power spectra across all measurement locations. This representation of the data clearly shows the presence of content at higher frequencies in the boundary layer, which then reduces in the freestream. The data near the floor is likely affected by the floor partially blocking the FLDI beams.

assumption the PSD's for each channel were then normalized by the average power measured in the frequency range between DC and 100Hz.

After checking for phase wrapping, the first validation performed for each data set was a comparison of the measured signal to the background noise data set as well as a comparison of the spectra obtained between subsequent data sets. As represented in Fig. 4.2, a high signal-to-noise ratio was achieved for all channels and the data remained highly consistent between the collected data sets. The only noticeable exception to the trends mentioned above can be seen in the PSD's for the 0.5mm measurement locations as seen in Fig. 4.1. The large reduction in signal-to-noise ratio at this position is largely attributed to the significant attenuation created by the floor cutoff. Particularly at this location, nearly all of the signal light is cut off by the tunnel floor. Even at this position, however, a signal-to-noise ratio of approximately 15dB is maintained in the frequency range between 1 and 250 kHz. Comparisons showing the trends in spectral content as the measurement location increases in the wall normal direction can be seen in Fig. 4.3 and Fig. 4.5. Noticeably, the trends in spectral intensity can be seen to progress smoothly without any noticeable discontinuities. Strong agreement is also seen between the upstream and downstream arrays as should be expected for the 3mm streamwise spacing. Once again, the measurements taken at the first wall normal location for each array represent the main exception to these trends.

Further validation of the measured spectra was carried out through a comparison of the results with accepted fluid dynamic theory. Turbulent boundary layer theory for fully developed turbulence suggests that an approximation (Eq. (4.1)) of the characteristic peak

frequency, f_c, can be determined from the ratio of the freestream flow velocity, U_∞, and boundary layer height, δ [21, 22].

$$f_c \sim U_\infty/\delta \tag{4.1}$$

A more detailed discussion of the freestream velocity and boundary layer measurements is provided in Section 4.2. For the current discussion, it is sufficient to note that the measured values for U_∞ and U_δ were approximately 498 m/s and 10.7 mm respectively. These values correspond to a characteristic frequency of approximately 45 kHz, which agrees with the frequency peaks for channels located inside the boundary layer as seen in Fig. 4.3 - 4.5. It is also expected that the peaks associated with the characteristic frequency will drop off in power and flatten out as the measurement location progresses out of the boundary layer and into the freestream [21, 22]. Agreement with this predicted theory can be seen in Fig. 4.3 and 4.5. Similarly, Fig. 4.5 shows an expected reduction in high-frequency turbulence content as the measurement locations approach and enter the freestream. Finally, as governed by the characteristic frequency and the Kolmogorov microscales in turbulent flow, a characteristic roll-off in spectral energy should be visible in the high-frequency power spectra. This phenomenon is a result of the turbulent energy cascade where energy is deposited from the flow into large eddies associated with the characteristic frequency. The energy from these large eddies is then decomposed into progressively smaller eddies as the flow progresses. Eventually, the energy associated with the smallest scale eddies will give way to dissipation

as heat. The Kolmogorov scales mentioned previously describe those scales at which the energy dissipation into heat dominates. The result is a large turbulence scale dominated by absorption of energy from the fluid flow which gives way to a smaller scale dominated by energy dissipation as heat. The resulting "overlap" region transitioning between these two dominating processes is characterized by a high-frequency roll-off with a $\frac{-5}{3}$ slope. Agreement with this theory can be seen in Fig. 4.4 where the high-frequency roll-off is shown to match this expected $\frac{-5}{3}$ power law for fully developed turbulence.

4.2 Velocity Measurements

The primary motivation for this work was the expansion of the existing LA-FLDI configuration created at UTSI [15] to include the capability of multi-point velocimetry measurements. As mentioned before, a primary motivator for selecting the UTSI Mach 2 facility to carry out these tests was the previous characterization that had been carried out in previous works. In particular, this work will make use of PIV measurements taken of the test section boundary layer by Kocher *et al.* [19]. Those measurements will be used as the primary validation of the Dual LA-FLDI velocimetry measurements taken here. A mean boundary layer flow field from that work can be found in Fig. 4.6 and the resulting boundary layer velocity profile can be found overlaid with many of the plots that will be discussed later on in this work.

The principles governing the measurement of flow velocity using the current LA-FLDI configuration are the same as those used with a standard Dual FLDI configuration. As

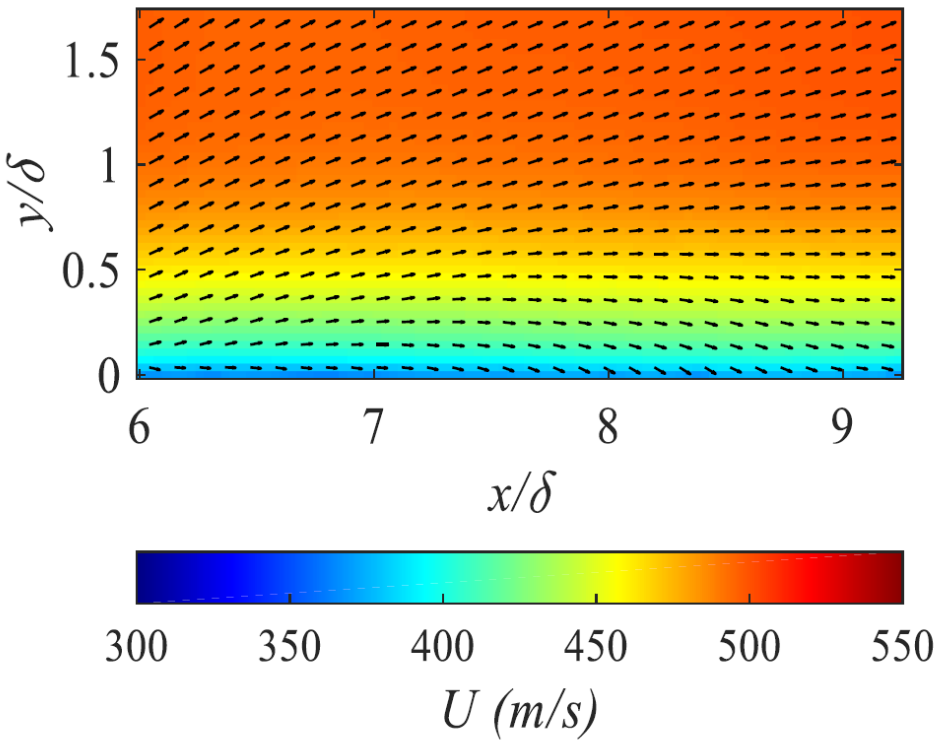

Figure 4.6: Mach 2 PIV velocity field measurements [19].

such, the velocity profiles collected in this work will employ techniques similar to those used previously by others [6, 7]. The method itself is relatively straightforward and the principle uses one of the oldest and simplest methods for calculating the velocity of an object, namely the division of distance traveled by the amount of time required for the trip. As mentioned in the description of the experimental setup, an accurate measurement of the distance between the two columns of the LA-FLDI setup is a crucial step in carrying out the velocimetry calculations. That distance (3.034mm in the case of this work) will be the traveled distance that is measured. Now, the only parameter left to find is how long it takes the flow to traverse between the two columns of the LA-FLDI. To determine this time differential, each probed location within a single LA-FLDI column is paired with the measurement location of the opposite column corresponding to the same wall-normal position. Because of the relatively small distances between the two columns of the LA-FLDI configuration, Taylor's hypothesis can be used to assume frozen turbulence. This implies that both columns of the LA-FLDI configuration should nominally record the same signal with the only difference between them being a time delay associated with the convective velocity. In reality, for multiple reasons including the approximate nature of Taylor's hypothesis as well as the non-continuous nature of realistic measurements, the measured signals will not be exact duplicates but should exhibit very similar patterns. A cross-correlation analysis then becomes an ideal tool for determining the best fit time delay between the two signals. Note that this technique requires both channels in a given pair to be measured simultaneously so care should be taken to ensure

that multiplexing is not employed by the data acquisition system selected. Once cross-correlation analysis was performed for each of the FLDI channel pairs, the resulting peak correlation value and associated lag could obtained. This lag represents the sampling offset between the given signals that corresponds to the highest agreement. Since the sampling rate, f_s, of the data acquisition system is a known quantity, the sample lag N_{lag} can be converted into a time lag between the two signals. In conjunction with the measurement pair spacing, S_{mp}, that lag is used to determine the flow velocity as shown in Eq. (4.2).

$$v = \frac{S_{mp}}{N_{lag}/f_s} \tag{4.2}$$

A plot of measurements obtained using this technique can be found in Fig. 4.7. This figure shows the normalized boundary layer profile and velocity measurements for each of the 24 locations measured overlaid with their estimated error bounds. The boundary layer velocity profile obtained from previous PIV measurements is also included on this plot for reference. As can be seen, there is a strong agreement between the values measured in this work and previous PIV measurements. This plot does however provide a good example of the large discretization/low resolution that can occur when using FLDI for velocimetry measurements and is one of the key limitations that needs to be considered when using this technique. Because of the non-continuous nature of the sampled data, the correlation analysis can only provide lag values for discrete offsets, shifting the data one sample location at a time. Since the measurement distance and sampling rate are fixed values, this results

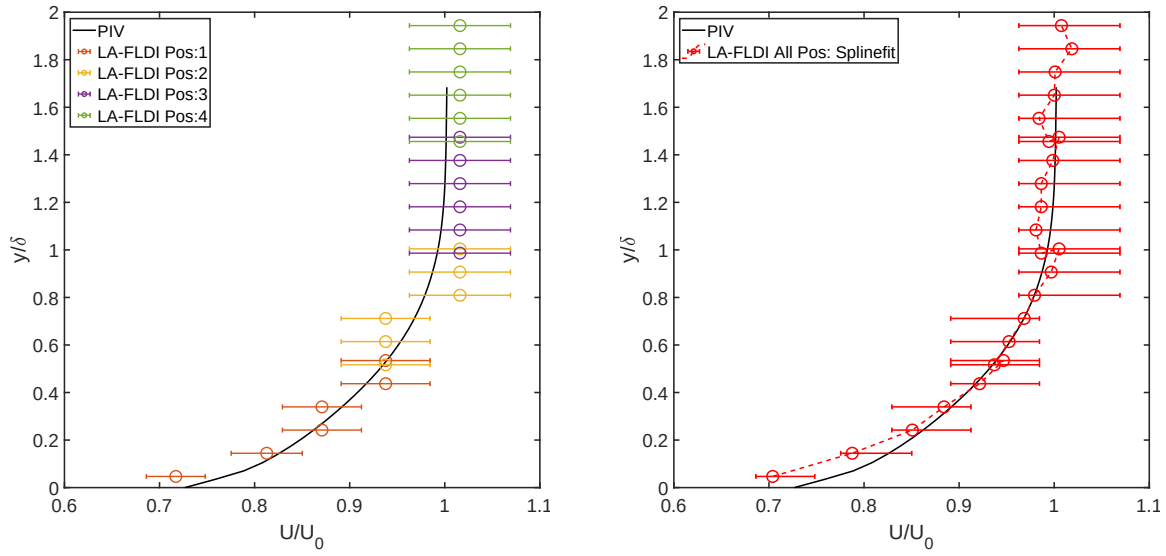

(a) Raw Velocities

(b) Correlation Spline Fit Velocities

Figure 4.7: Dual LA-FLDI velocity profiles showing error bounds compared with reference PIV data.

in discrete jumps for the possible calculated velocities. Additionally, the difference between these discrete steps will increase along with velocity. For the freestream velocities presented in Fig. 4.7 the difference between possible output velocities is approximately 39 m/s. This relationship can be seen graphically in Fig. 4.8.

In order to improve on the resolution provided by the LA-FLDI velocity measurement, a curve fit was applied to the computed correlation values in the region of the correlation peak. Once the peak correlation had been identified for each measurement location, a cubic spline interpolation was calculated for the region between the lag values on either side of the peak correlation. Once calculated, a new peak location could be found for the resulting spline. This new peak was then used to obtain a higher resolution velocity estimate. A plot of the correlation values and resulting spline fits for several measurement locations can be found in Fig. 4.9. This work does not explore any possible improvements in accuracy or uncertainty bounds that might be provided by this or similar methods and so all values calculated using this method will be shown plotted against the original non-fitted uncertainty bounds. Nevertheless, this method does provide an improvement in resolution that is 100 times greater than could be obtained directly with our system and sampling rate. Figure 4.7b provides a plot of these interpolated velocity measurements. In this plot, it can be seen that the interpolated values provide a closer fit to the previous PIV measurements than was obtained with the raw correlation calculations. Likewise, the interpolated values follow the expected power law shape for turbulent boundary layer profiles as would be expected. Note

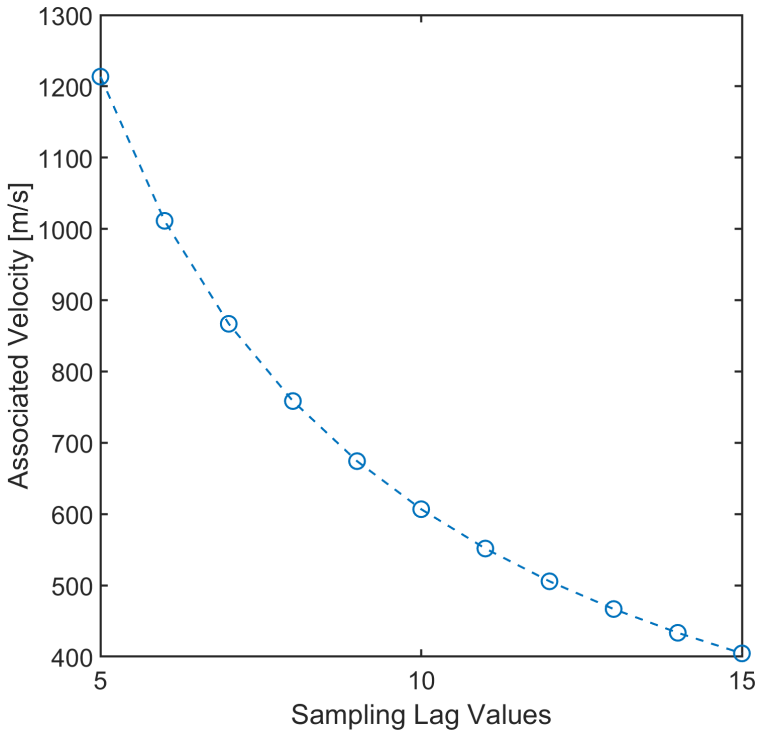

Figure 4.8: Representative plot showing the discrete possibilities for velocity measurements that can be obtained based on the sampling rate and pair spacing of the current LA-FLDI setup.

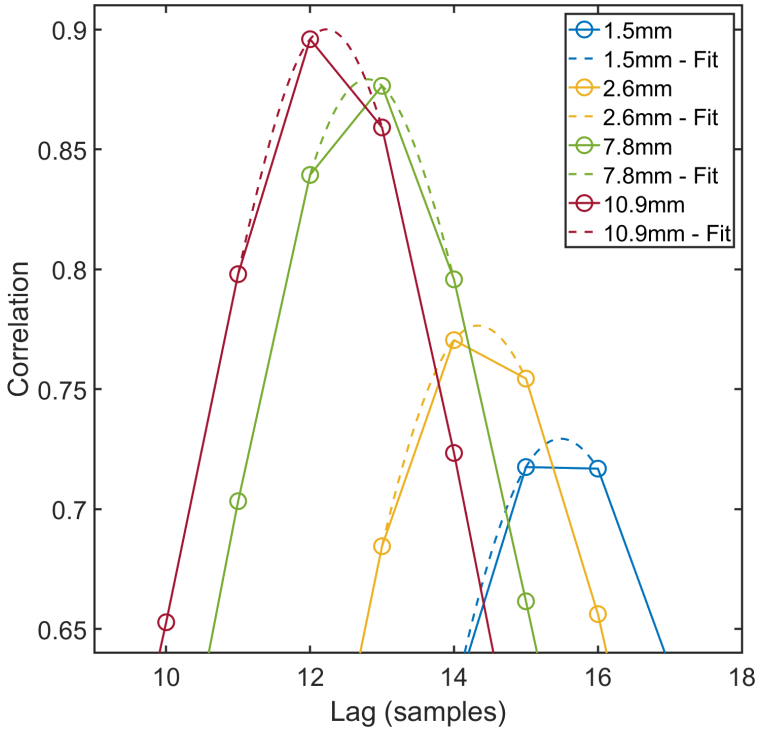

Figure 4.9: Calculated correlation values shown plotted in the regions of peak correlation for several measurement locations. The fitted spline used for velocity interpolation is also shown here.

as well that all interpolated values still fall within the expected error bounds of the raw measurements (a discussion on uncertainty can be found in section 4.4).

Once the velocities had been calculated for each measurement location, they could then be used to determine the freestream velocity, U_0, and estimated boundary layer height, δ. Determination of an estimated U_0 value was relatively straightforward. For this calculation, the velocity measurements obtained at the final setup position (approx. 15.5mm - 20.5mm) were assumed to be entirely in the freestream based on previous measurements of the boundary layer height in the UTSI M2 facility. Had these previous measurements not been available for this experiment, an extra setup position could easily have been added to the testing matrix near the centerline of the tunnel. The measured values from the upper six wall normal heights were then averaged to obtain an estimated U_0 value of 497.8 (m/s). This measurement falls within 1% of the 501.1 (m/s) value from previous PIV measurements [19]. Determination of the boundary layer height was based on the measured location of the U_{99} edge velocity (velocity corresponding to 99% of the freestream velocity, U_0). In order to determine this location, a smooth polynomial fit was applied to the measured velocities across all locations. The boundary layer height, δ was then defined to be the location along the fit line where the velocity reached the U_{99} value. The resulting value for the boundary layer was calculated to be δ =10.6mm. Fig. 4.10a details the described method used for the determination of U_0 and δ. The associated LA-FLDI polynomial curve fit for velocity can also be seen overlaid with the associated uncertainty bounds and the PIV profile in Fig. 4.10b.

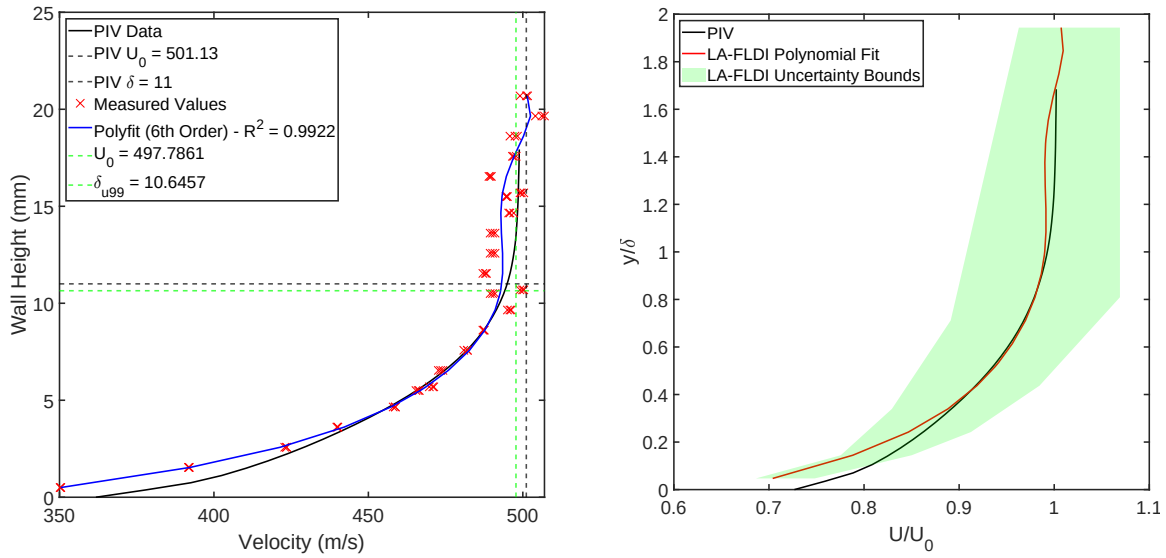

(a) U_0 and U_{99} Estimation

(b) LA-FLDI fit curve vs. PIV

Figure 4.10: Dual LA-FLDI velocity profile with 6^{th}-order polynomial fit used to determine U_0 and U_{99}. Reference PIV data shown for comparison.

Cerruzi *et al.* also describes another method for boundary layer approximation based on a comparison of the RMS signal values obtained at each measurement location [23]. A comparison of calculated RMS values for each measurement location can be found in Fig. 4.11 overlaid with the previously calculated boundary layer height and referenced against a power spectra surface plot with the same height scale. It can be seen from this figure that this RMS method of data visualization shows good agreement between both the measured boundary layer height and the measured power spectra.

In the same work Cerruzi *et al.* describe a potential application of FLDI velocimetry by running the raw FLDI signals through bandpass filters in order to isolate the measured convective velocity for different turbulence scales. In that work, the authors cite an assertion by Owen [24] which states that "small-scale fluctuations are convected with the local mean velocity (U_l); however, as the scale increases, the more U_c/U_l differs from unity." The bandpass filtered data obtained by Cerruzi *et al.* [23] show agreement with Owen's assertion with velocity measurements decreasing away from the expected values at lower frequencies. The authors do note however that this phenomenon can also be attributed to the reduced signal rejection for low frequency disturbances in the unfocused portion of the FLDI beams. This could result in an additional component in the FLDI signal obtained from the low frequency and slower moving disturbances present at the sidewalls of the tunnel. Similar measurements were taken using the data from the current work and can be seen in Fig. 4.12. A similar reduction in measured velocities is clearly present but the deviations seen in this work are mainly limited to frequency bands below 20 kHz with the strongest variations

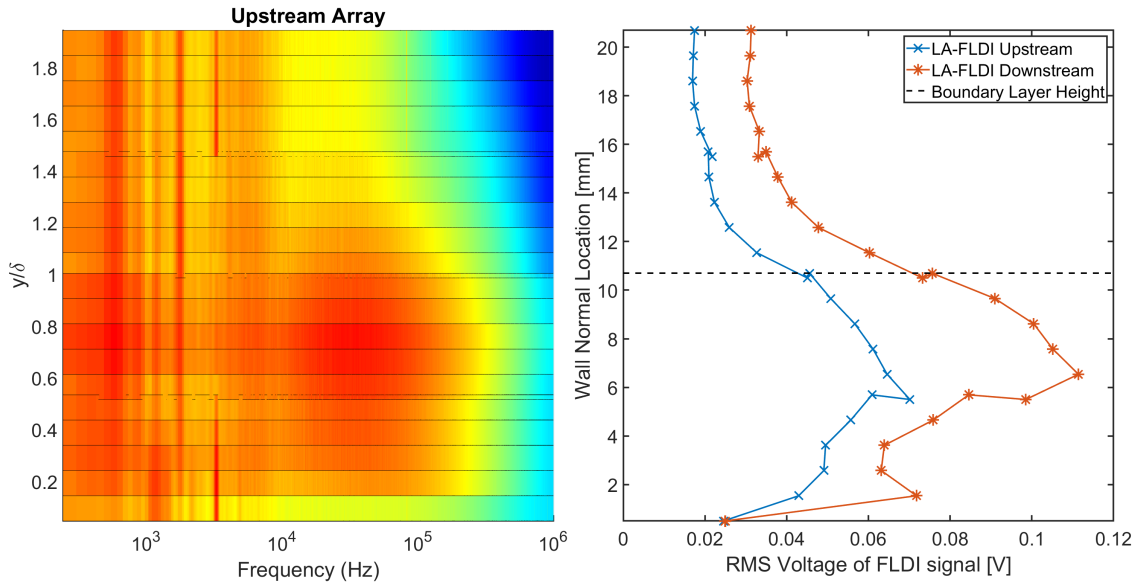

Figure 4.11: A colormap showing normalized power spectra across all measurement locations is shown on the left with a plot showing the raw signal values at each location shown on the right.

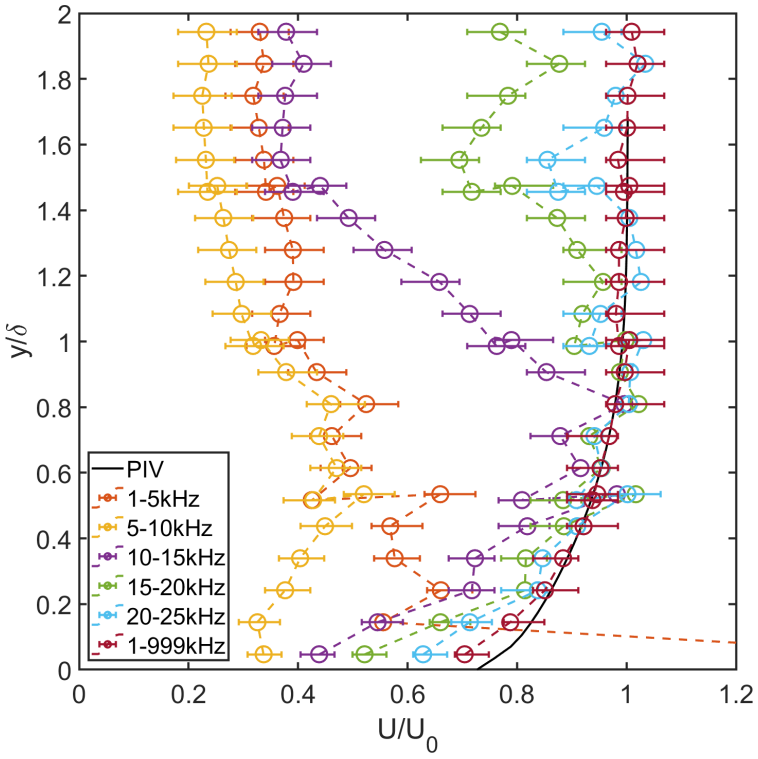

Figure 4.12: Dual LA-FLDI velocity profiles showing the effect of bandpass filtering of the raw signals for various frequency bands. The PIV velocity profile is also included for reference.

seen in measurements taken in the freestream. These results seem to indicate a higher likelihood that the majority of this variation would be attributed to poor signal rejection of the low-frequency sidewall disturbances rather than variation in the convective velocity with turbulence scales. In any case, as noted by Ceruzzi, this phenomenon merits further consideration and could be explored in more detail in future works.

Overall the agreement between the Dual LA-FLDI velocimetry and PIV measurements was found to be consistent with the values that would be expected when using a standard Dual FLDI system in a single measurement point configuration. It can also be seen that there is no noticeable variability in the sensitivity or accuracy between each of the LA-FLDI channel pairs. The deviations from the predicted measurements near the freestream and tunnel floor can likely be attributed to decreased signal fidelity in those regions as is typical for FLDI measurements. Near the freestream, decreasing density fluctuation intensity and turbulence scale bandwidth both contribute to lower correlation confidence between FLDI pairs and therefore more variance in measured values. Likewise, measurements in close proximity to the floor will have a majority of their signal attenuated by the obstruction of the floor. This attenuation similarly decreases the confidence in the correlation thereby increasing variability in the data albeit not to the degree seen in freestream data.

4.3 Application in Non-Standard Boundary Layers

While not included in the original scope of this work, a pair of extra tests were carried out to take advantage of the existing setup and extra tunnel availability. The motivation for these

tests was to better understand if the velocity profile obtained with LA-FLDI was capable of showing an adverse pressure gradient shape and also to test if correlations could still be made with significant surface roughness. These tests represent an exploratory investigation into these effects and as such the results should be regarded only as a proof of concept requiring further validation in future testing.

The first configuration aimed to test velocity profile measurements in and around a separation shock associated with a downstream obstruction in the flow. This test was carried out with a 2.54 cm diameter and 7.5 cm tall vertical cylinder attached to the tunnel floor, as shown in Fig. 4.13a. According to previous schlieren imaging of the same setup, the separation was expected to occur approximately 2.1 diameters upstream of the cylinder. The LA-FLDI array was configured to be at this location (2.1 diameters upstream) with the lowest measurement position set to 0.5mm above the tunnel floor. The velocity profile measured from this experiment can be seen in Fig. 4.14a. The profile indicates a significant slowing of the flow and does bear resemblance to the velocity profile of flow that is subject to an adverse pressure gradient. A more carefully controlled experiment will be needed to fully explore whether FLDI-based velocimetry is capable of indicating flow separation or extremely adverse profile shapes. However, the data here suggests that it may have the sensitivity required to carry out such measurements. Another consideration for such a measurement would be the difficulty in correlating the signals in slow or even reversed flow near separation. In these regions, the frozen flow assumption required for adequate correlation between the measured beam pairs may no longer hold true. In these regions,

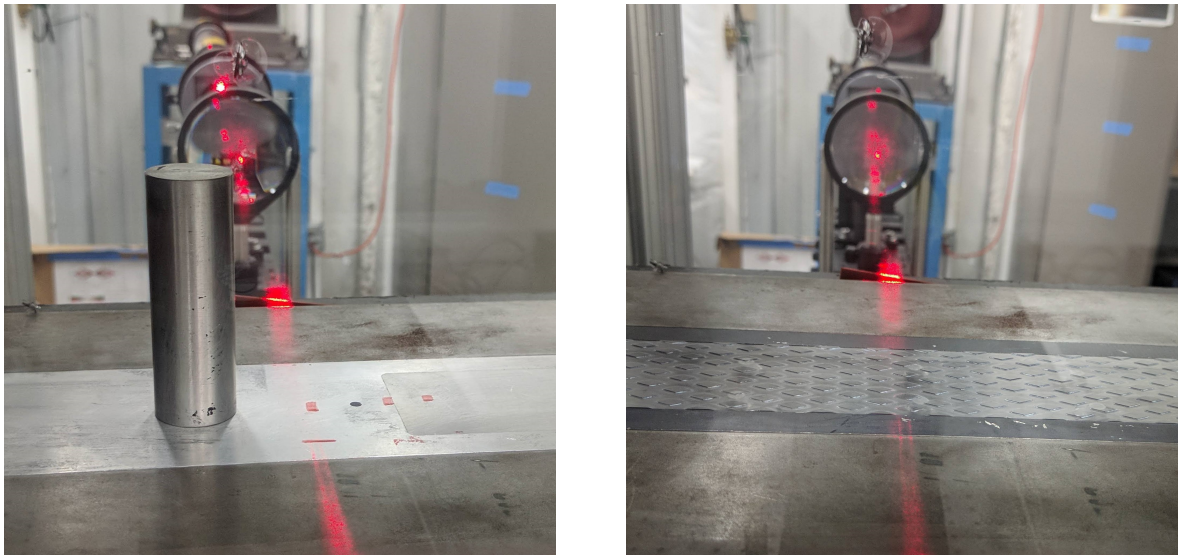

(a) **(b)**

Figure 4.13: Test-section configurations for non-standard boundary layer investigation. (a) Measurements of the boundary layer profile near the separation shock associated with a turbulent shockwave-boundary layer interaction (SBLI) produced by a vertical cylinder. (b) Measurements over distributed diamond-shaped roughness with $k/\delta = 0.03$.

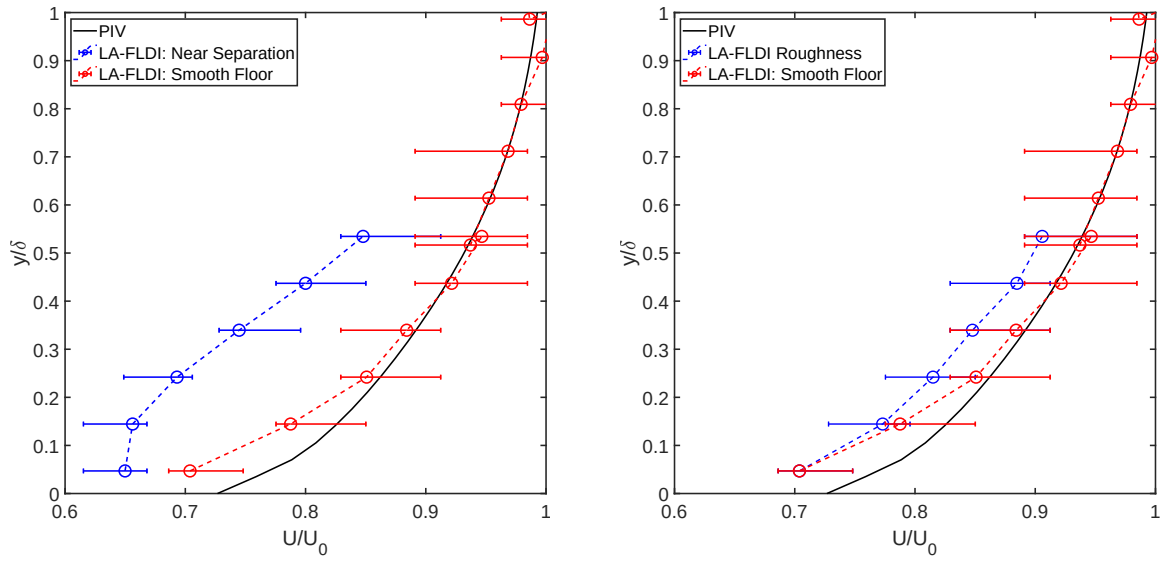

Figure 4.14: Dual LA-FLDI velocity profiles for additional tests. (a) The velocity profiles found near the separation shock compared to the base flow data and original base flow PIV. (b) A plot showing the velocity profile over the distributed diamond roughness compared with the smooth wall data and smooth wall PIV data.

a smaller beam pair spacing may be required in order to obtain accurate and meaningful results. In such a case, a 2D grid like that discussed by Gragston *et al.* [7] may be the best option. This method would allow for expanded spacing in regions of high velocity in order to maintain sufficient resolution. Closer beam pairs could then be chosen for cross-correlation in regions with slower flow (e.g. near the wall).

The second non-standard configuration tested was that of a boundary layer over a rough surface. For this test, a diamond roughness floor insert with a $k/\delta = 0.03$ [19] was installed in the tunnel floor. An image of this setup can be seen in Figure 4.13b. The measured velocity profile from the floor roughness test can be seen in Fig. 4.14b, with a comparison against the smooth floor LA-FLDI profile and the previous PIV measurements. Similar to the separation experiment, the profile appears to show a general slowing of the velocities which follows the expected response for a turbulent boundary layer above a rough surface. Further testing and validation will be required, but initial results indicate that FLDI can still be used for velocimetry over distributed roughness without any concern that the roughness is invalidating Taylor's frozen turbulence hypothesis. Additional work on this topic should explore the effects k/δ has on the ability to correlate disturbances, potentially finding a critical value for which correlations can no longer be utilized. Additionally, a direct comparison to PIV or molecular tagging velocimetry should be done to further validate the technique in these use cases.

4.4 Uncertainty Analysis

The uncertainty analysis for the velocity measurements follows the law of propagation of uncertainty as detailed in the NIST guidelines for evaluating uncertainty [25]. As mentioned previously, the velocity is determined by dividing the FLDI measurement pair spacing, S_{mp}, by the correlation delay time, t_{corr}. The two dependent variables of S_{mp} and t_{corr} will need to have individual uncertainties defined in order to pass them into the uncertainty propagation. For this work, the total uncertainty in the column pair spacing was defined to be twice the single FLDI beam pair spacing, S_{bp}. The reasoning behind this choice lies in the fact that each FLDI beam pair represents a single differential measurement. Therefore, the location of a disturbance propagating between the two beams of a single FLDI measurement location cannot be resolved inside the spacing of those beam pairs. Because the spacing between velocity measurement pairs includes the uncertainty from two individual FLDI beam pairs, the total included range of the uncertainty becomes $2 * S_{bp}$. The resulting single direction uncertainty in S_{mp} can then be defined as shown in Eq. (4.4). The range of uncertainty in t_{corr} is dominated by the sampling rate of the signal. For a sampling rate approaching a continuous signal, other effects such as the accuracy of the correlation calculation as well as signal delays introduced by the data acquisition hardware would also influence the timing uncertainty. For the purposes of this work, however, these effects are expected to be negligible in comparison to the sampling period. Therefore the total included range of uncertainty in t_{corr} is defined as the sampling interval, $\frac{1}{f_s}$. The resulting single-sided uncertainty can

then be defined as shown in Eq. (4.5). Per the NIST guidelines for the propagation of uncertainty, partial derivatives of the driving equation must then be taken with respect to each of the independent variables. A root sum square uncertainty is then obtained by summing the products of the squared uncertainty from each independent variable and the associated partial derivative for the governing equation. The equations for this uncertainty propagation are detailed in Eq. (4.3) - (4.8) below. As a result of the squared denominator and typical delays of $t_{corr} << 1$ uncertainty resulting from the data acquisition sampling rate becomes the primary driver for the uncertainty of most FLDI velocimetry measurements.

$$v = \frac{S_{mp}}{t_{corr}} \tag{4.3}$$

$$u(S_{mp}) = S_{bp} \tag{4.4}$$

$$u(t_{corr}) = \frac{1}{2 * f_s} \tag{4.5}$$

$$(\frac{\partial v}{\partial S_{mp}})^2 = \frac{1}{t_{corr}} \tag{4.6}$$

$$(\frac{\partial v}{\partial t_{corr}})^2 = \frac{-S_{mp}}{t_{corr}^2} \tag{4.7}$$

$$u_c^2(v) = u^2(S_{mp}) * (\frac{\partial v}{\partial S_{mp}})^2 + u^2(t_{corr}) * (\frac{\partial v}{\partial t_{corr}})^2 = (\frac{S_{mp}}{t_{corr}})^2 + (\frac{S_{bp}}{2 * f_s * t_{corr}^2})^2 \tag{4.8}$$

Chapter 5

Conclusions

As a continuation of previous works carried out at UTSI using the LA-FLDI technique [7, 15], the goal of the experiments presented in this work was to prove the feasibility of expanding the single-column LA-FLDI configuration for use as a dual column LA-FLDI instrument. The data and calculations presented in this work have shown that the selected configuration could be successful in obtaining multiple simultaneous spectra and velocity measurements in a supersonic flow. These results detailed previously have shown that the Dual LA-FLDI configuration functioned as well as a single location dual FLDI setup. The collected data and measurements also saw a strong agreement with previous measurements and characterization of the turbulent boundary layer on the test section floor of the UTSI Mach 2 facility. As further substantiation of the Dual LA-FLDI technique, the spectral and velocimetry data also matched closely with the basic theoretical expectations for fully developed turbulent boundary layers in a supersonic flow as seen in the M2 facility. Furthermore, this technique quickly proved its validity for one of the stated goals of improving testing efficiency, an achievement that should not be overlooked. All of the testing and measurements that were taken for the primary campaign were able to be completed in only a few hours of testing completed over the course of a single afternoon. In that time, it was possible to obtain a

measurement profile nearly twice the boundary layer height of our facility with high spatial fidelity in the wall-normal direction. The collected data includes 48 discrete FLDI data points with 24 corresponding velocity measurement locations. Accounting for the 3 independent data sets collected per setup location, a total of 144 unique data sets were obtained (192 including background noise measurements). Based on previous campaigns carried out in this facility, obtaining measurements with this level of spatial fidelity and range could take a week or more to complete with a traditional FLDI setup. This improved testing efficiency will prove to be particularly important for future work carried out in impulse facilities commonly used in hypersonic flow research such as the UTSI Mach 4 and Mach 7 facilities. In these facilities, measurement translation is not feasible within the duration of a single run and cycle times can limit testing to 3 or 4 setup changes per day. For high-cost-per-run facilities such as the UTSI Mach 7, this improvement in efficiency will also result in a significant reduction in the costs associated with carrying out a particular measurement campaign. Even blowdown facilities similar the UTSI Mach 2 can benefit from this configuration by eliminating the need for complicated translation setups and allowing for compressed experimental campaigns with a resulting increase in tunnel availability.

5.1 Future Work

The Dual LA-FLDI configuration used in this work was shown to be fully functional, however, there are several areas in this current iteration that could see improvement in future works. The first of these possible adaptations involves possible substitutions for the additional

Wollaston prism used to obtain the second column of LA-FLDI measurement locations. It is expected that this optic could easily be replaced with a secondary diffractive optic acting in tandem with the first. These two diffractive optics could then be selected to provide measurement arrays with any combination of rows and columns. The row and column spacing could also be easily modified with the selection of diffractive optics with varying divergence angles. While it would also be feasible to use a single MxN pattern diffractive optic to achieve similar results, this approach is not recommended as it places a limit on the achievable geometries. The dual diffractive optic configuration used in tandem with the existing Wollaston prisms allows for independent control over the array orientation and skew as well as the orientation of the individual beam pairs. That capability has proven to be useful when testing on angled models or surfaces with the single column LA-FLDI configuration and it is expected that similar benefits would be realized here. This effect can be seen in Fig. 5.1.

Per the previous discussions on the velocimetry uncertainty calculations, the main driver of uncertainty for the current technique lies in the capture of the intensity signal and the associated sampling rate of the data acquisition system. This limitation results in the current data acquisition rate of 2 MHz being a key area for potential improvement in the system. The high channel counts necessary for LA-FLDI make high-speed oscilloscopes impractical for data collection and other high-speed data acquisition systems can become the primary driver of cost and complexity of the system. Current procurement efforts are underway to obtain a data acquisition capable of improved sampling rates. The new system will be a

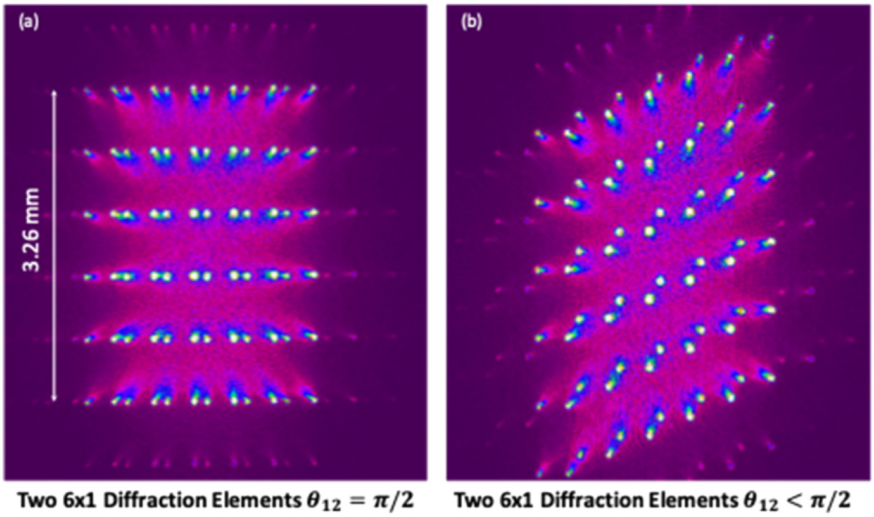

Figure 5.1: (a) MxN matrix of FLDI grid points created using two diffractive optical elements placed in series. (b) Rotation of the second diffractive element relative to the first results in a transformation of the square grid into a parallelogram (orientation of individual beam pairs can be controlled independently via the Wollaston prism angle) [15].

Spectrum Instruments digitizerNetbox (Part Number: DN2.592-16) which will be capable of simultaneously recording 16 channels with a sampling rate of 20MS/s/ch. This sampling rate will provide a significant boost to the capabilities of the LA-FLDI system. Care should be taken however to consider the bandwidth of other system components. As an example, for the gains selected on the Thorlabs PDA36A2 photodetectors used in this experiment, the diodes themselves were limited to 1 MHz bandwidth. While the roll-off at this frequency will not be instantaneous, there would be little use in sampling the current setup at 20 MHz. On the contrary, for the high channel counts seen in this experiment, data processing could already be seen to be taxing for a standard desktop workstation. It is therefore prudent that the trade-off between measurement resolution and data processing requirements be taken into careful consideration when selecting a signal sampling rate.

While there are certainly many other improvements that could be made to the current system, the final recommendation provided in this text will be in relation to the current methodology used for collecting and converting the signal light into a usable electrical signal. One of the ongoing challenges presented by LA-FLDI is the high density of optical signals requiring measurement. The current configuration relies on a complex coupling of the output light through an array of collimators into fiber optic cables. This setup can be particularly sensitive to the angles of the incoming beams relative to the optical axis of the collimators leading to complications in alignment and in some cases increased sensitivity to vibrations. Extra optical components also contribute to additional light losses and limit the signal-to-noise ratios that can be obtained. This method also results in a high part count assembly

with a delicate and bulky setup that would not be well suited for expansion to larger arrays as can be seen in Fig. 5.2a. Work by Chism *et al.* has shown that imaging the output beams of the LA-FLDI directly onto a high-speed camera can provide useful and accurate data [26]. This technique is highly limited however by the achievable data acquisition rates. At the time of this writing, the upper limit for high-speed camera frame rates is in the range of 1-2 MHz. Even then, the limited pixel resolution at these speeds leads to alignment difficulty and limited options for LA-FLDI array configurations. Camera systems capable of these frame rates also come with significant price tags often exceeding $100k. It is possible however that future advancements in camera technology could make this the ideal solution for LA-FLDI measurements. Another solution presented here is the creation of a custom multi-diode array with circuitry for providing diode bias and amplification provided from remote boards. A prototype of this arrangement is detailed here. The array uses multiple switchable gain OEM photodetector packages (Thorlabs PDAPC1) which have had the photodetectors removed from the board and replaced with a short length of shielded twisted pair cable. The opposite ends of the cables are connected to TO-5 photodiode sockets (Thorlabs STO5P) which are themselves soldered onto a breadboard in a compact equally spaced linear arrangement. The array uses the same Si photodiodes originally paired with the amplifier board (Thorlabs FDS100). Power is supplied to the amplifiers from a +/-12V DC power supply (e.g. TRACO TML 40212C). Signals are then carried from the amplifier boards to the data acquisition system using MMCX to BND adapter cables (Thorlabs CA3339). The prototype assembly

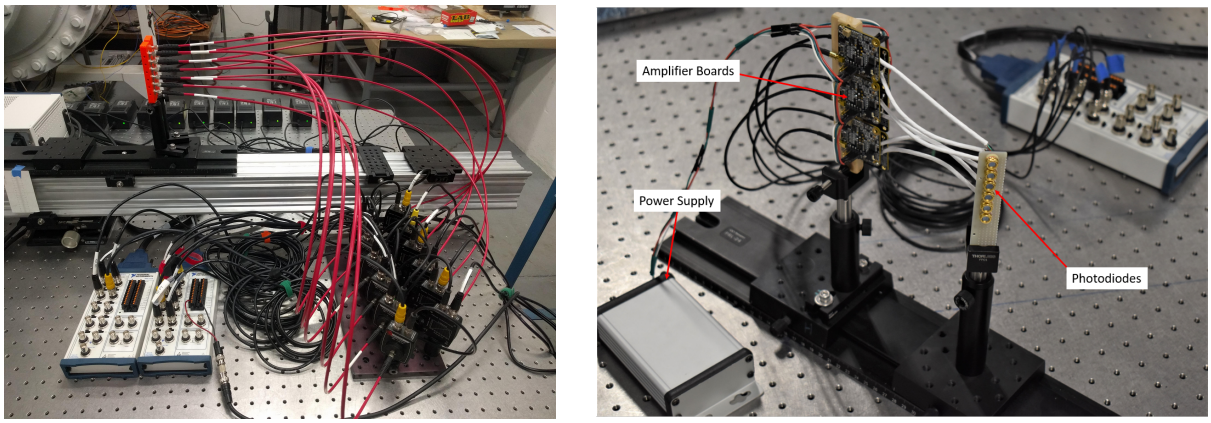

(a) **(b)**

Figure 5.2: (a) Current fiber optic array based signal collection for LA-FLDI measurements. (b) Prototype multi-diode array with remote amplification circuitry.

can be seen in Fig. 5.2b where the simplification of this system over the previous fiber optic arrangement can be plainly seen.

Preliminary testing with the new array was carried out using the laser scatter from a Spectra Physics Quanta Ray Nd:YAG laser. The laser was configured to supply single-shot laser pulses with expected pulse widths of 3-10ns and an output wavelength of 532nm. In order to limit the saturation of the photodiodes, the output of the laser was directed into a beam dump and an additional beam blocking panel was placed between the measurement location and beam dump. Simultaneous measurements of the resulting laser scatter were then taken on both the prototype LA-FLDI array and a Thorlabs PDA36A2 amplified photodetector (the same used in the current fiber optic configuration). A picture of the experimental setup can be seen in Fig. 5.3. The photodiode responses were recorded using a Teledyne waveSurfer10 oscilloscope with a 1GHz data acquisition rate with channel resolutions set to 20 mV/div and 100 ns/div. Measurements were collected at both 0dB and 20dB amplifier gains. Plots of the resulting impulse responses can be found in Fig. 5.4. While further characterization will be required for the response of the new array, these preliminary findings show excellent correlation between the existing photo-amplifiers and the new array assembly. In future works, the prototype array will be updated to use custom manufactured printed circuit boards and to improve on the cable shielding and system packaging. It is hoped that the resulting instrument will provide a compact 1x6 photodiode array that can be easily grouped into larger arrays of any required size.

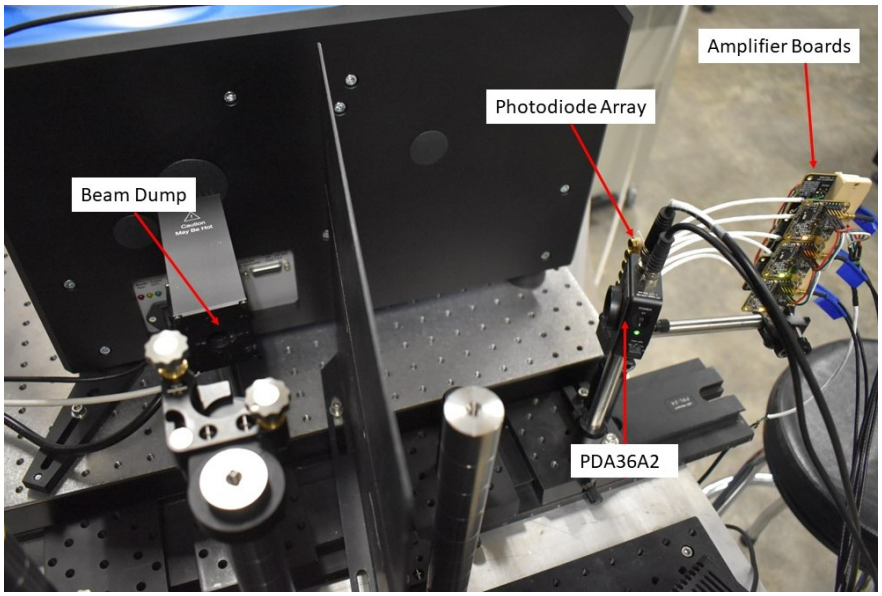

Figure 5.3: Experimental setup for comparison of the impulse response between the new prototype photodiode array and a standard Thorlabs PDA36A2 amplified detector. To limit saturation, the laser pulse was fired into a beam dump with an additional panel placed between the beam dump location and the photodetectors.

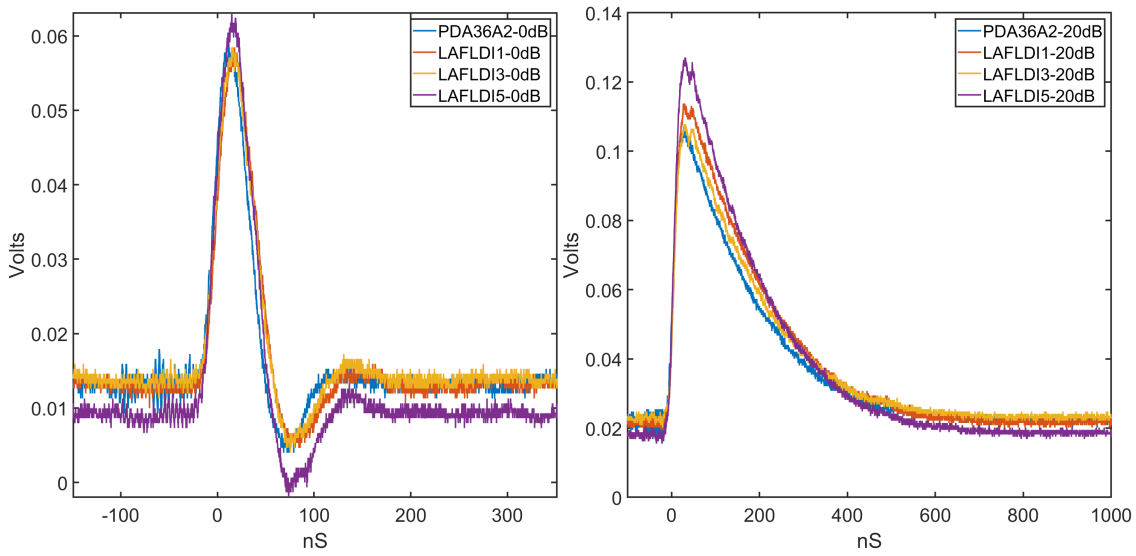

Figure 5.4: Photodiode responses of a standard PDA36A2 amplified detector and the new prototype photodiode array to laser scatter from an Nd:YAG laser. (a) Signals were measured with amplifier gains set to zero for all channels. (b) Signals were measured with amplifier gains set to 20 dB on all channels.

Bibliography

[1] Steven P Schneider. Developing mechanism-based methods for estimating hypersonic boundary-layer transition in flight: The role of quiet tunnels. *Progress in Aerospace Sciences*, 72:17–29, 2015. 1, 2

[2] JCR Hunt, PA Durbin, and X Wu. Interactions between freestream turbulence and boundary layers. *Annual Research Briefs*, pages 113–124, 1998. 2

[3] Matthew R Fulghum. *Turbulence measurements in high-speed wind tunnels using focusing laser differential interferometry*. The Pennsylvania State University, 2014. 2, 3, 9, 10

[4] Gary S Settles and Matthew R Fulghum. The focusing laser differential interferometer, an instrument for localized turbulence measurements in refractive flows. *Journal of Fluids Engineering*, 138(10), 2016. 2

[5] HG Hornung and NJ Parziale. Spectral characteristics of pitot noise. In *International Symposium on Shock Waves*, pages 409–414. Springer, 2013. 3

[6] Andrew Ceruzzi and Christopher P Cadou. Simultaneous velocity and density gradient measurements using two-point focused laser differential interferometry. In *AIAA Scitech 2019 Forum*, page 2295, 2019. 4, 10, 38

[7] Mark Gragston, Theron J. Price, Kirk Davenport, John D. Schmisseur, and Zhili Zhang. An m by n fldi array for single-shot multipoint disturbance measurements in high-speed flows. In *AIAA Scitech 2021 Forum*, 2021. doi: 10.2514/6.2021-0599. 4, 12, 38, 53, 57

[8] G Smeets and A George. Laser-differential interferometer applications in gas dynamics. Technical report, INSTITUT FRANCO-ALLEMAND DE RECHERCHES SAINT-LOUIS (FRANCE), 1996. 4, 5

[9] G Smeets and A George. Gas-dynamic investigations in a shock tube using a highly sensitive interferometer. Technical report, INSTITUT FRANCO-ALLEMAND DE RECHERCHES SAINT-LOUIS (FRANCE), 1996. 5

[10] G Smeets and A George. Laser-interferometer with phase compensation. Technical report, INSTITUT FRANCO-ALLEMAND DE RECHERCHES SAINT-LOUIS (FRANCE), 1996. 6

[11] Bryan E Schmidt and JE Shepherd. Analysis of focused laser differential interferometry. *Applied optics*, 54(28):8459–8472, 2015. 8, 9, 10

[12] NJ Parziale, JE Shepherd, and HG Hornung. Observations of hypervelocity boundary-layer instability. *Journal of Fluid Mechanics*, 781:87, 2015. 10

[13] Brett F Bathel, Joshua M Weisberger, Gregory C Herring, Rudolph A King, Stephen B Jones, Richard E Kennedy, and Stuart J Laurence. Two-point, parallel-beam focused laser differential interferometry with a nomarski prism. *Applied optics*, 59(2):244–252, 2020. 10

[14] NJ Parziale, JE Shepherd, and HG Hornung. Free-stream density perturbations in a reflected-shock tunnel. *Experiments in Fluids*, 55(2):1–10, 2014. 10

[15] Mark Gragston, Theron Price, Kirk Davenport, Zhili Zhang, and John D. Schmisseur. Linear array focused-laser differential interferometry for single-shot multi-point flow disturbance measurements. *Opt. Lett.*, 46(1):154–157, Jan 2021. doi: 10.1364/OL.412495. 12, 36, 57, 60

[16] Mark Gragston, Farhan Siddiqui, and John D. Schmisseur. Detection of second-mode instabilities on a flared cone in Mach 6 quiet flow with linear array focused laser differential interferometry. *Experiments in Fluids*, 62(4):81, April 2021. doi: 10.1007/s00348-021-03188-6.

[17] Farhan Siddiqui, Mark Gragston, William S Saric, and Rodney DW Bowersox. Mack-mode instabilities on a cooled flared cone with discrete roughness elements at Mach 6. *Experiments in Fluids*, 62(10):1–13, 2021. 12

[18] Joshua M Weisberger, Brett F Bathel, Gregory C Herring, Gregory M Buck, Stephen B Jones, and Angelo A Cavone. Multi-point line focused laser differential interferometer for high-speed flow fluctuation measurements. *Applied Optics*, 59(35):11180–11195, 2020. 13

[19] Brian D Kocher, Christopher S Combs, Phillip A Kreth, and John D Schmisseur. Characterizing the streamwise development of surface roughness effects on a supersonic boundary layer. In *2018 Fluid Dynamics Conference*, page 4047, 2018. 13, 14, 36, 37, 44, 53

[20] A. Pope and K.L. Goin. *High Speed Wind Tunnel Testing*. Wiley, 1965. ISBN 9780471694021. URL https://books.google.com/books?id=yHFTAAAAMAAJ. 16

[21] William S Saric. Turbulent boundary layers in subsonic and supersonic flow (les couches limites turbulentes dans les ecoulements subsoniques et supersoniques). Technical report, ADVISORY GROUP FOR AEROSPACE RESEARCH AND DEVELOPMENT NEUILLY-SUR-SEINE ..., 1996. 35

[22] Hendrik Tennekes, John Leask Lumley, Jonh L Lumley, et al. *A first course in turbulence*. MIT press, 1972. 35

[23] Andrew Ceruzzi, Braeden Callis, Daniel Weber, and Christopher P Cadou. Application of focused laser differential interferometry (fldi) in a supersonic boundary layer. In *Aiaa scitech 2020 forum*, page 1973, 2020. 46

[24] FK Owen and CC Horstman. On the structure of hypersonic turbulent boundary layers. *Journal of Fluid Mechanics*, 53(4):611–636, 1972. 46

[25] Barry Taylor and C Kuyatt. Guidelines for evaluating and expressing the uncertainty of nist measurement results 1994 edition, 1994-09-01 1994. 54

[26] James R Chism, Mark Gragston, Scott J Peltier, and Thomas A McManus. Measurements of a Mach 2.3 turbulent boundary layer using high-speed imaging of linear array-fldi. In *AIAA AVIATION 2022 Forum*, page 3474, 2022. 62

[27] Kirk Davenport and Mark Gragston. Simultaneous turbulent boundary layer velocity profile and scalar turbulence spectra with linear array-fldi. In *AIAA SCITECH 2022 Forum*, page 1313, 2022.

Appendices

A Fundamental Matlab Scripts

Included below are the critical matlab sub-scripts used for reducing the data presented in this text.

A.1 PSD Code

```
function [PSD,PSDnorm,F] = fldiSpec(Data,fs,hnum)
function [PSD,PSDnorm,F] = fldiSpec(Data,fs,hnum)
pl = true;
run˙count = size(Data,3);
fnorm = 100;
Win= hanning(floor((size(Data,1))/hnum));
PSD = zeros(floor(max(256,2^nextpow2(length(Win)))/2)+1,size(Data,2),run˙count);
PSDnorm = PSD;
F = PSD;
for j = 1:run˙count
for i = 1:size(Data,2)
data = Data(:,i,j)-mean(Data(:,i,j));
[PSD(:,i,j),F(:,i,j)] = pwelch(data,Win,[],[],fs);
PSDnorm(:,i,j) = PSD(:,i,j)/mean(PSD(F(:,i,j)¡=fnorm,i,j));
end
if pl
figure('WindowState','maximized');
plot(F(:,:,j),PSD(:,:,j),'LineWidth',1.6)
set(gca,'YScale','log','XScale','log')
set(gca,'LineWidth',1.8,'FontSize',18)
xlim([500,fs/2])
xlabel('Hz')
legend()
title(['Run ' num2str(j)])
end
end
end
```

A.2 Velocity Correlation Code

```
function [Max,Dt,Coef,lag,V,Vs,uc] = fldiCorr(Data,fs,pairs,Bsp)
pl = false;
```

```
run˙count = size(Data,3);
MSdata = Data-mean(Data);
maxlag = ceil(100e-6*fs);
Dt = zeros(size(pairs,1),run˙count);
Max = Dt;
V = Dt;
Vs = Dt;
uc = Dt;
Coef = zeros(2*maxlag+1,size(pairs,1),run˙count);
lag = Coef;
for j = 1:run˙count
if pl
t9 = figure('WindowState','maximized'); hold on;
ax = gca;
end
for i = 1:size(pairs,1)
 a = pairs(i,1);
b = pairs(i,2);
[Coef(:,i,j),lag(:,i,j)] = xcorr(MSdata(:,a,j),MSdata(:,b,j),maxlag,'coeff');
[Max(i,j),Loc] = max(Coef(:,i,j));
Dt(i,j) = lag(Loc,i,j)/fs;
V(i,j) = pairs(i,3)/Dt(i,j);
% Spline Corr Fit
xs = lag(Loc-1,i,j):.01:lag(Loc+1,i,j);
Cf = interp1(lag(:,i,j),Coef(:,i,j),xs,'spline');
[˜,LocS] = max(Cf);
Vs(i,j) = pairs(i,3)/(xs(LocS)/fs);
% Uncertainty Calculation
uc(i,j) = sqrt((Bsp^2)*(1/Dt(i,j))^2+((1/(2*fs))^2)*(pairs(i,3)/(Dt(i,j)^2))^2);
if pl
color = ax.ColorOrder(ax.ColorOrderIndex,:);
plot(lag(:,i,j),Coef(:,i,j),'o-','Color',color,'MarkerSize',15,'LineWidth',2)
plot(xs,Cf,'--','LineWidth',2,'Color',color)
xlabel('Lag (samples)')
ylabel('Correlation')
box on; axis square;
set(gca,'LineWidth',2,'FontSize',24);
legend();
end
end
end
if pl
```

```
    condSaveFig(t9,['CorrelationsWFits']);
end
end
```

A.3 Freestream Velocity and Boundary Layer Thickness Estimation

```
if ~exist('Data','var')
load('211015˙M2˙DLAFLDI-0-20mm-2Mhz-4x12ch-Combined-x4.mat')
end
initHardVals
PIV = load('KocherPIV.mat');
lw = 2;
ms = 15;
font = 24;
[pairs,x,xs,xn,xsn,cs] = initPairs(steps,sO,r,VSp,Sp,Pos1,delta);
%% Get/Plot NI Data
[Max,Dt,Coef,lag,V,Vs,~] = fldiCorr(Data(:,:,2:size(Data,3)),fs,pairs,Bsp);
%% Get U0 from freestream average
U0 = mean(Vs((steps-1)*r:r*steps,:),'all');
U99 = U0*0.99;
for i = 1:size(Vs,2)
Vels(size(Vs,1)*(i-1)+1:size(Vs,1)*i,1) = Vs(:,i);
pos(size(Vs,1)*(i-1)+1:size(Vs,1)*i,1) = x(:);
end
[pos, idx] = sort(pos);
Vels = Vels(idx);
%% Find delta with U99 and spline fit
figure('WindowState','maximized');hold on;
set(gca,'LineWidth',lw,'FontSize',font)
% PIV Data
plot(PIV.meanBy,PIV.Y,'k','LineWidth',lw,'DisplayName','PIV Data');
xline(PIV.Uo,'k--','DisplayName',['PIV U˙–0″ = ' num2str(PIV.Uo)],'LineWidth',lw)
yline(PIV.delta,'k--','DisplayName',['PIV “delta = ' num2str(PIV.delta)],'LineWidth',lw)
% LAFLDI Data
plot(Vels,pos,'rx','MarkerSize',ms,'DisplayName','Measured Values');
for i = 6
[fo,S] = polyfit(pos,Vels,i);
[pV,error] = polyval(fo,pos,S);
r2 = 1 - (S.normr/norm(pV - mean(pV)))^2;
delta = fzero(@(pos) polyval(fo,pos)-U99,10);
plot(pV,pos,'b','DisplayName',['Polyfit (6th Order) - R^2 = ' num2str(r2)],'LineWidth',lw)
```

```
xline(U0,'g--','DisplayName',['U˙–0″ = ' num2str(U0)],'LineWidth',lw)
yline(delta,'g--','DisplayName',['"delta˙–u99″ = ' num2str(delta)],'LineWidth',lw)
end
legend('Location','northwest')
ylabel('Wall Height (mm)')
xlabel('Velocity (m/s)')
box on; axis square
```

A.4 Initialization Variables

```
% NI - Setup
spacing = load('SpacingValues.mat'); % Load spacing values (um)
deltaUo = load('deltaUoValues.mat');
fs = 2e6; % Sampling Frequency Hz
Sp = spacing.Psp/1e6; %m LA-FLDI column spacing (velocity pairs)
r = 6; % Number of LA-FLDI rows
VSp = spacing.Vsp/1e3; %mm LA-FLDI space between rows
Bsp = spacing.Bsp/1e6; % (m) LA-FLDI space between individual beams in pairs
Pos1 = 0.5; % mm height of lowest point
steps = 4; % # of setup heights
sO = 5; % Increment between setups (mm)
delta = deltaUo.delta; % Boundary Layer Height (mm)
U0 = deltaUo.U0; % Freestream Velocity (m/s)
```

A.5 Beam Spacing Calculation

```
%Import Beam Profiler Images
BP = load('BP.mat').BP; % properly exposed for analysis
BPHE = load('BPhe.mat').BP; % high exposure image for display
BPh = BP;
pix = 7.38; % um/pixel
% Surface Plot of Beam Profile
figure;
a = surf(BP);
a.EdgeColor = 'none'; hold on;
% Find Profile Peaks
maskaa = imregionalmax(BP);
BP = BP.*maskaa;
% Extract 24 highest peaks representing beam center locations
[B,I] = maxk(BP(:),24);
[r,c] = ind2sub(size(BP),I);
% Plot peaks to confirm
plot3(c,r,B,'r+')
```

```
% Calculate beam spacings
peaks = [c r B];
peaks = sortrows(peaks,2,'ascend');
for i = 1:6
peaks((4*i-3):(4*i),:) = sortrows(peaks((4*i-3):(4*i),:),1,'ascend');
coord = peaks((4*i-3):(4*i),1:2);
if i¡6
Vspace(i,:) = [pix*pdist(peaks([(4*i+1) (4*i-3)],1:2)) ...
pix*pdist(peaks([(4*i+2) (4*i-2)],1:2)) pix*pdist(peaks([(4*i+3)...
(4*i-1)],1:2)) pix*pdist(peaks([(4*i+4) (4*i)],1:2))];
end
Pspace(i,:) = [pix*pdist(coord([1 3],:)) pix*pdist(coord([2 4],:))];
Bspace(i,:) = [pix*pdist(coord(1:2,:)) pix*pdist(coord(3:4,:))];
end
Vsp = mean(Vspace,'all'); % Vertical spacing between rows
Psp = mean(Pspace,'all'); % Spacing between velocimitry pairs
Bsp = mean(Bspace,'all'); % Inner beam pair spacing
```

A.6 Data File Examples

deltaU0Values.mat	
U0	497.7861
delta	10.6457
pV	72x1 double - Polynomial fit velocity vector
pos	72x1 double - Polynomial fit position vector

SpacingValues.mat	
Bsp	96.0109
Psp	3.0344e3
Vsp	1.0382e3

BP.mat and BPHE.mat	
BP	724x964 double - Intensity values for each beam profiler pixel
BPHE	724x964 double - Intensity values for each beam profiler pixel

KockerPIV.mat	
Uo	501.13
Y	1x49 double - PIV wall-normal position values
delta	11
meanBy	1x49 double - PIV wall-normal velocity values

211015_M2_DLAFLDI-0-20mm-2MHz-4c12ch-Combined-x4.mat	
Data	2e6x48x4 double - FLDI Voltages arranged as Timestep x Location x Run Case

Vita

Kirk M. Davenport received his Bachelor of Science degree in mechanical engineering in 2012 from the University of Utah. Following graduation he spent six years performing controls and mechanical design work for Jacobs Technology in Tullahoma, TN. In 2018 he began working for the Horizon Research group at the University of Tennessee Space Institute where he manages operations in the TALon laboratory and provides engineering support for the design and fabrication of new facilities and experiments.